**Suleiman, Shawqi Mohammad**

STRESS INTENSITY FACTORS FOR NEAR SURFACE CRACKS BY BOUNDARY COLLOCATION

*Iowa State University* PH.D. 1986

**PLEASE NOTE:**

In all cases this material has been filmed in the best possible way from the available copy. Problems encountered with this document have been identified here with a check mark __✓__.

1. Glossy photographs or pages _____
2. Colored illustrations, paper or print _____
3. Photographs with dark background __✓__
4. Illustrations are poor copy _____
5. Pages with black marks, not original copy _____
6. Print shows through as there is text on both sides of page _____
7. Indistinct, broken or small print on several pages __✓__
8. Print exceeds margin requirements _____
9. Tightly bound copy with print lost in spine _____
10. Computer printout pages with indistinct print _____
11. Page(s) _____ lacking when material received, and not available from school or author.
12. Page(s) _____ seem to be missing in numbering only as text follows.
13. Two pages numbered _____. Text follows.
14. Curling and wrinkled pages _____
15. Dissertation contains pages with print at a slant, filmed as received __✓__
16. Other _____

_____

_____

# Stress intensity factors for near surface cracks by boundary collocation

by

Shawqi Mohammad Suleiman

A Dissertation Submitted to the
Graduate Faculty in Partial Fulfillment of the
Requirements for the Degree of
DOCTOR OF PHILOSOPHY

Department: Engineering Science and Mechanics
Major: Engineering Mechanics

Approved:

Signature was redacted for privacy.
In Charge of Major Work

Signature was redacted for privacy.
For the Major Department

Signature was redacted for privacy.
For the Graduate College

Iowa State University
Ames, Iowa

1986

TABLE OF CONTENTS

# I. INTRODUCTION

Failure at stress magnitudes below design values remain the biggest problem facing designer today. This early failure is most likely due to the existence of flaws, voids, arc burns, notches, and cracks which are introduced during the many stages of manufacturing and fabrication or may develop later under service conditions. Although it would be ideal to eliminate all flaws through better control over the causes which produce them, it is more economical to accept the inevitability of defects and to study the means of detecting and estimating the remaining useful life when they are present.

To estimate different tolerance levels, it is necessary to find the fracture criteria the engineer can use in his or her design. Fracture Mechanics introduced new concepts like the J-integral and the stress intensity factor. These fracture criteria can predict the conditions for crack propagation and life of a structure when a flaw is present.

The introduction of these fracture criteria, J-integral and the stress intensity factor, did not make all problems easier for only selected cases yield to analytical solutions. Numerical solutions can handle many more problems, but suffer from difficulties such as dealing with complex geometry, importance of correct boundary conditions, etc. They also require separate modeling for each problem. It is hard to verify the solutions and is difficult to achieve convergence and stability.

In the absence of a numerical solution or to verify one, the experimental approach is often needed. In this regard, photoelasticity

is attractive because it gives a full field solution to the fracture problem. It also can handle plane problems as well as three-dimensional problems through model slicing. Other experimental techniques are also available. These include Moire', interferometry, speckle, caustics and scattered light methods.

Experimental methods have their own difficulties, such as the need for suitable modeling materials when it is not possible to conduct the study on the actual material of interest. By combining numerical and experimental techniques, the investigator can gain a good understanding of fracture mechanics.

The purpose of this research is to determine the mixed mode stress intensity factors from photoelastic data taken along a boundary close to the crack tip when strong interaction is present. The method is based on boundary collocation of a stress function for an interior crack. Combining collocation with the use of half fringe photoelasticity (HFP), permits the collocation scheme, through automatic and precise measurement of very low fringe orders, to correctly extract the required fracture parameters $K_I$ and $K_{II}$. Satisfying exactly the state of stress at a number of points on the segment of boundary interacting with the crack tip avoids the region close to the crack tip where nonlinear effects are present. This reduces the influence of the crack root radius which is present when slits are used instead of real cracks and also eliminates the need to exactly locating the crack tip.

Furthermore, at the low stresses that can be used with half fringe photoelasticity, linear elastic fracture mechanics (LEFM) is more likely to apply than in most other experimental methods. Under these

conditions, the boundary collocation method should provide a more accurate prediction of the two stress intensity factors, $K_I$ and $K_{II}$. Another advantage of this method is the development of a linear system of equations which is easy and fast to solve, because it does not have the nonconvergence to which most other overdeterministic methods are prone.

## II. LITERATURE REVIEW

In 1913, Inglis [1] determined the stresses around an elliptical hole in an infinite plate under uniaxial tension. By changing the ratio of the minor axis, b, to the major axis, a, the solutions for a circular hole, b/a = 1, or a fine crack, b/a = 0, can be obtained. He showed that for an ellipse, the maximum tensile stress occurs at the end of the major axis and has a value of $\sigma[1+2a/b]$ (where $\sigma$ is the far field nominal stress). This gives the typical stress concentration value of 3 for a circular hole in an infinite plate. If the major axis makes an angle $\beta$ with the direction of applied tension, he noticed that the maximum stress does not occur at the end of the major axis. The stress at this end is $\sigma[a/b-\cos 2\beta(1+a/b)]$. Inglis also discussed the stresses resulting from different notches which can be thought of as ellipses with the minor axis taken as $b=\sqrt{(a\rho)}$ (where $\rho$ is the notch root radius). This choice produces a stress at the notch of the form $\sigma[1+2\sqrt{(a/\rho)}]$. The last conclusion was shown applicable to a square hole with rounded corners, as well as to a deep edge crack or deep notch.

Later, Griffith [2] attempted to explain why the rupture theory of the 1920s failed to predict the fracture of materials under loads that are well within the elastic range. He found definite links between early failure and surface treatments such as filing, grinding, or polishings. He found that the existence of scratches in turned specimens could reduce the strength as much as 50% when compared to polished ones. Griffith further noticed that the maximum fracture strength possible before failure depended upon the shape, size, and the

loading conditions to which a crack was subjected. To explain this phenomenon, Griffith adopted the "theorem of minimum energy." The new rupture criteria, which he proposed, required that for the crack to remain in equilibrium, the potential energy of the whole system should continuously decrease as the system passes from the unbroken to the broken state. The work done against the cohesive forces on either side of the crack appears as potential surface energy. If the crack size is larger than the radius of molecular action, the energy per unit surface area is a material constant commonly known as surface tension $\gamma$. Using Inglis' work, Griffith determined that according to the new criteria, $\sigma \sqrt{a}$ should be a constant equal to $\sqrt{(2E\gamma/\pi\nu)}$ in plane stress (where E is the modulus of elasticity; $\gamma$ is the surface tension of the material; a is the crack length; $\nu$ Poissons's ratio, and $\sigma$ is the breaking stress). He confirmed the energy principal with his work on scratches in glass. The theoretical limit, for plane stress, $\sigma = \sqrt{(2E\gamma/\nu\pi a)}$, leads to a very high fracture strength which is approached in mono crystals and single strands of materials. In practice, the fracture strength is much smaller than this prediction.

In 1933, Westergaard [3] used the mathematical theory of elasticity to study edge cracks in reinforced concrete under bending and compressive stresses. He treated the two surfaces of a crack as two large cylinders in contact and assumed that stresses in front of each crack tip is of the same shape as that of the contact pressure (ellipse) of the two cylinders. Hollister [4] used photoelasticity to test Westergaard's work, by applying a compressive force ahead of the crack tip. The stresses observed with this type of loading do not show high

stress concentrations, except when the applied force line of action passes very close to the crack tip. In a later paper, Westergaard [5] examined a variety of harmonic (analytic) functions and showed their suitability to describe the stress field for a restricted, yet useful, class of problems such as bearing pressures and a central crack in Mode I loading.

In a different approach Williams [6] studied the influence of various boundary conditions on the stress singularity for angular corners of different angles. He assumed homogeneous boundary conditions which restrict the solution to long cracks where the circumferential boundaries are greater than several plate thicknesses. Later, in an experimental investigation, Post [7] gave a complete solution for a stationary long edge crack. He achieved stress separation by combining photo-elasticity with interferometry. The results indicate large deformations at the crack tip which cause diversions of the light field. This divergence at the crack tip was apparent by the lack of interference patterns in this area. Post's paper is the earliest experimental evidence of the existence of large deformations and, possibly, a triaxial state of stress at the crack tip. The paper also indicates that the shape of the photoelastic fringe loops far from the tip depends on the loading conditions, while closer ones seemed to be independent of loading conditions far from the crack tip. This work also confirms Inglis' finding that the maximum stress did not occur on the axis of symmetry of the inclined crack, which may explain the direction at which cracks propagate.

Theocaris and Pazis [8], using both mechanical stylus measurements

and the method of caustics, found large out-of-plane deformations near the crack tip. They also found that the plate buckled above and below the crack line under mixed loading conditions. The method of caustics is itself based on the existence of such large deformations, that a divergent lens is produced around the crack tip. The caustic is a singular curve formed by the interference of the divergent light that passes the zone of large deformation in a transparent material around the crack tip (transmitted caustic) and/or by the interference of the reflected light from the same region (reflected caustic) with a reference light beam. The size and shape of the area bounded by the caustic curve is related to the magnitude of the stress intensity factors. In dynamic studies and for Mode I loadings, the area is proportional to $K_I$ and can be easily estimated optically. Continuous measurement of $K_I$ SIF is very easy, which makes caustics very appealing, especially in dynamic studies.

The Griffith [2] energy approach for crack propagation led Irwin [9], in 1957, to postulate a stress intensity factor (SIF) criterion. The feature of SIF, whereby a characteristic is evaluated not at the crack tip, but rather from the stress field in a zone close to the crack tip, together with the availability of Irwin's singular solution for this zone, led to the popularity to this criterion. A large volume of results on SIFs has been compounded in references 10, 11, and 12.

The application of photoelasticity to plane problems was used in the evaluation of Mode I ($K_I$) stress intensity factors in the work of Post [7], Irwin [9], and Wells and Post [13]. Stress freezing and slicing techniques were employed by Fessler and Mansell [14], Marloff et

al. [15], and Schroedl et al. [16] to study three-dimensional problems. The freezing technique was developed for this by Smith [17,18] and Smith and Olaosebiken [19,20], for the determination of SIFs at cracks in the nozzles of nuclear reactors. An extensive literature review in the area of photoelasticity and stress freezing can be found in the thesis by Baek [21]. Smith et al. [22] discussed the nonlinear effects near crack tips in frozen models and Shroedl et al. [16] discussed the different factors influencing data collection in a stress frozen field.

Photoelasticity was further found useful in studying dynamic fracture problems as in the work of Bradley and Kobayashi [23,24] and Kobayashi and Ramulu [25,26]. A review by Wang [27] demonstrated that photoelasticity is useful in thermal stress loading, both steady states, and transient.

Many of the methods used in extracting SIFs are reviewed by [21,25,26,28,29]. The bulk of these methods rely on Irwin's singular solution. This is evident in Schroedl et al.'s differencing method [16], Smith and Olaosebikan's quadratic method [18, 19], Smith's extrapolation method [19], Bradley and Kobayashi's shear differentiating method [23], the Zero-isoclinic and maximum breadth methods described by Redner [28], Ruiz and Phang's slope method [29], Irwin's two-parameter method [30], Etheridge and Dally's three-parameter approach [31], Gdoutos and Theocaris' extrapolations method [32], and Marloff et al. stress concentration Method [33] used at the Westinghouse Company. By including only $K_I$ and $\sigma_{0x}$ [30] or $K_I$ and $K_{II}$ [19,32], these methods are limited solutions for the influence of the crack tip only. They ignore far field effects which can be strong in the presence of other cracks

and/or a boundary.

Applying the aforementioned methods gives inconsistent results. When applied to the same problem, Smith and Olaosebikan [19] showed that differences as large as 9% existed. Murthy et al.'s [34] compared both Broek's [35] analytic solution and Gross et al.'s [36] boundary collocation method for an edge crack in a finite rectangular plate to previously mentioned methods by Irwin, Bradley, and Kobayashi, and Shroedl, and Smith. The comparison showed poor results, except for a small crack length to plate width ratios. In addition to a lack of agreement, the singular solution results were shown to deviate greatly from the analytic results as the crack length to plate width ratio is increased. On the other hand, both the analytic solution [35] and the boundary collocation method [36] were shown to remain in good agreement up to 0.4 crack length to plate width ratio. The boundary collocation method was based on William's equations which included higher order terms. The study [34] shows that singular solution validity is limited to a ratio of crack length to plate width of .25. The inclusion of higher order terms in the series expansion of the stress functions was shown to give better results than the singular solution can give. These results clearly indicate the unsuitability of the singular solution, even when moderate interaction between a crack tip and a boundary exists.

The problem of crack interaction with a boundary was solved by Bradley and Kobayashi [24], Cheng [37], Sanford [38], and Sanford and Dally [39] by including higher order non-singular terms. The introduction of higher order terms in the stress functions expansion

allows data collection in the far field, while the singular solutions limit data collection to region in the immediate vicinity of the crack tip and on the closed loops of the isochromatic fringes. The closed loops near the crack tip was shown [7] to be independent of the loading conditions. This very close region near the crack tip is referred to by the invariant zone, which depends in size and shape on the singular terms only. The invariant zone exists between two other regions, the nonlinear zone which starts from the crack tip and terminates when the invariant zone begins. Finally, the far field region extends from the invariant region onwards.

The separation of the stress field into three regions is not always possible. In general, there is no definite separation between these three regions. Also, it has been noticed that as one crack interacts with another crack or a boundary, the invariant zone size becomes even smaller, which does not permit its identification. As the invariant zone become too small, only far field isochromatic loops which are dependent on the loading conditions becomes available for study. These far field isochromatic loops require the accurate estimation of the singular terms, as well as the higher order terms in stress functions.

The method of scattered light photoelasticity, as presented by Holmes et al. [40] and Ross et al. [41], adds a new dimension to experimental mechanics. This method does not require the tedious work of slicing and also preserves the model for repeated analysis as needed. It is limited, however, to cases where the light tensor suffers very little rotation in the direction of observation. Brillaud and Lagarde [42] have applied a related technique called "optical slicing" to

fracture problems in three-dimension, but its full potential is yet to be demonstrated.

Data collection in the far field requires more accurate means of estimating the fringe values, because the fringe orders are small so the relative error in their estimation may be high. They are also more susceptible to noise, which could mask their true value. Voloshin and Burger [43], Muller and Saackel [44], Tsai and Park [45] used image processing techniques to improve the accuracy of data collection. Image processing techniques make it possible to eliminate most of the noise present in the image, while at the same time improving the level of differentiating of the fringe order. A typical computer-based vision system can express 256 levels of light intensity between 0 and 1/2 fringe order. This is at least two orders of magnitude higher than could be achieved before. It is now possible to automate data collection by employing methods like half fringe photoelasticity (HFP) as described by Voloshin and Burger [43].

# III. THEORY

## A. Photoelastic Theory

Certain materials (polymeric plastics, resins, and to a lesser degree, glass) exhibit a temporary change in refractive index under stress conditions. In 1853, this change in refractive index was cited in [46] due to Maxwell, for linearly elastic materials, to be:

$$n_1-n_0=c_1\sigma_1+c_2(\sigma_2+\sigma_3)$$

$$n_2-n_0=c_1\sigma_2+c_2(\sigma_3+\sigma_1)$$

$$n_3-n_0=c_1\sigma_3+c_2(\sigma_1+\sigma_2)$$

where

$\sigma_1$, $\sigma_2$, $\sigma_3$ are the principal stresses at the point;

$n_0$ is the index of refraction of the unstressed material;

$n_1$, $n_2$, $n_3$ are the indices of refraction of the stressed material along the principal stress directions;

$c_1$, $c_2$ are the material stress-optic constants.

In terms of relative retardation, as light passes through the material in a direction normal to the model plane, the stress optic law can be reduced to [46]

$$\Delta = \frac{2\pi hc}{\lambda}(\sigma_1 - \sigma_2)$$

where

$\Delta$ is the relative retardation in brewsters (1 brewster = $10^{-13}m^2/N$ or $6.895\times10^{-9}$ $in^2/lb$);

c is $(c_2-c_1)$, a material stress-optic constant. The constant is shown by Vandaele-Dossche and Van Green [47] to be a function of wavelength in certain cases as the material passes from elastic to plastic state;

h is the distance the light passes through the model;

$\lambda$ is the wave length of light used;

$\sigma 1$, $\sigma 2$ are the in plane principal stress.

For practical reasons, the stress optic law is usually expressed as

$$\sigma_1 - \sigma_2 = \frac{Nf_\sigma}{h}$$

where

$N = \Delta/2\pi$ is the relative retardation in term of fraction wave length and is called fringe order;

$f_\sigma = \lambda/c$ in lb/in or N/m is material constant for a particular wavelength.

In a dark field polariscope, the light intensity, I, emerging from the analyzer of a circular polariscope, is related to relative retardation, $\Delta$, by

$$I = K \sin^2 \frac{\Delta}{2} \qquad (3.1)$$

where

K is a constant.

In this configuration, light extinction (i.e., I=0) takes place when

$$\frac{\Delta}{2} = N\pi \quad \text{for } N = 0, 1, 2, \ldots$$

where

N is the fringe order and the resulting dark lines are the isochromatic fringes.

Another special case is the light field setup. Here, the intensity is

$$I = k \cos^2 \frac{\Delta}{2} \tag{3.2}$$

and extinction takes place when

$$\frac{\Delta}{2\pi} = \frac{2n+1}{2} \text{ for } n = 0, 1, 2, \ldots$$

In general, the Tardy compensation method [46] gives the equation for the light intensity for an arbitrary position of the analyzer. The light intensity emerging from the analyzer is given by

$$I_\alpha = K(1 - \cos 2\alpha \cos\Delta - \cos 2\gamma \sin 2\alpha \sin\Delta) \tag{3.3a}$$

where

I is the emerging light intensity;

$\alpha$ is the angle between the analyzer axis in the arbitrary position and the dark field position;

K is a constant;

$\gamma$ is the isoclinic angle; and

$\Delta$ is the relative retardation.

If the analyzer is rotated by +/- 90 degree, the emerging light intensity is

$$I_{\alpha \mp 90} = K(1 + \cos 2\alpha \cos\Delta + \cos 2\gamma \sin 2\alpha \sin\Delta) \tag{3.3b}$$

Adding the previous two equations (3.3a,3.3b), we obtain

$$I_\alpha + I_{\alpha \mp 90} = 2K$$

or

$$K = (I_{\alpha}+I_{\alpha\mp 90})/2 = I_o$$

where

$I_o$ is a constant, independent of the loading conditions of the model.

The $I_o$ serves as a reference intensity. Its value is defined as K when this value is constant over the field of interest. It is the average value for K, if K varies but the variation in the region of collecting data might be small. If variations in K are large, a point-by-point calibration is needed. This would require the measurement of separate reference intensities for all data points. The value for K is influenced by variations in model transmissibility of light, light source variations, and aberrations in the optical elements.

A plot of intensity vs fringe order is shown in Figure 3.1 for dark field and in Figure 3.2 for light field. Based on intensity alone, these plots clearly indicate that Eqs. (3.1) and (3.2) can only be used to measure fringe orders less than half order. To extend the working range of the Eqs. (3.1,3.2), it is necessary to manually segment the region of collecting data in half order ranges (i.e., $0 < N < 0.5$, $0.5 < N < 1.0$,...).

The method of half fringe photoelasticity (HFP) [43] capitalizes on the ability of the image analysis system, the "EyeCom System," to distinguish between 256 gray levels in any half order range. To automate the data collection procedures, the HFP requires that the range of fringe orders to be collected lies between 0. and 0.5 [21,27,43,48, 49].

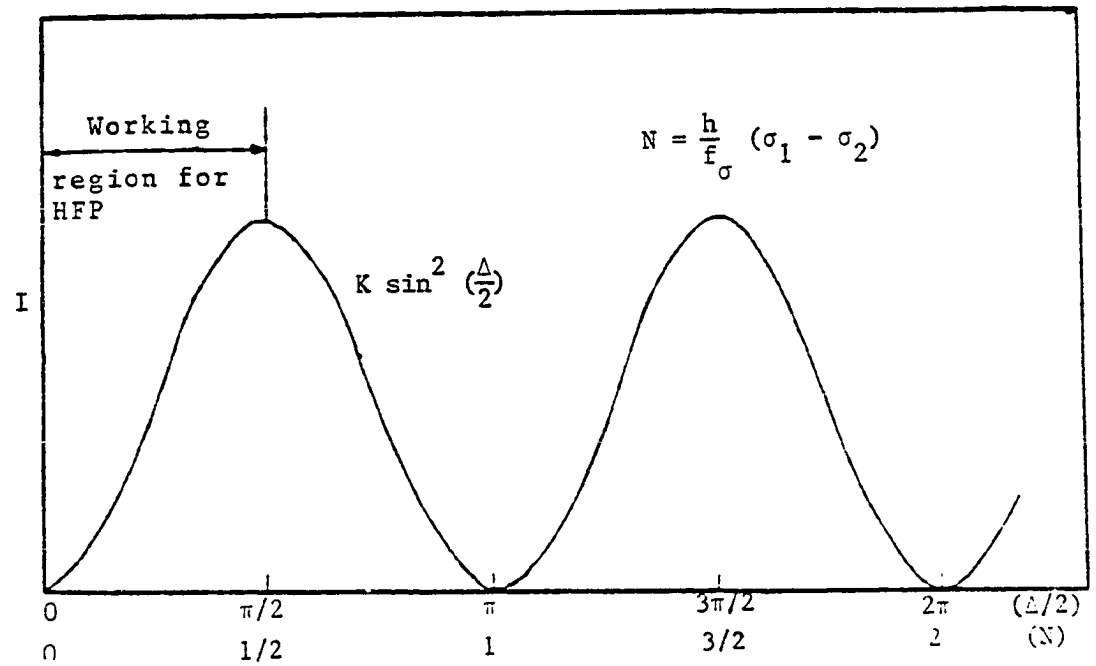


Figure 3.1. Intensity vs retardation plot for a dark field circular polariscope

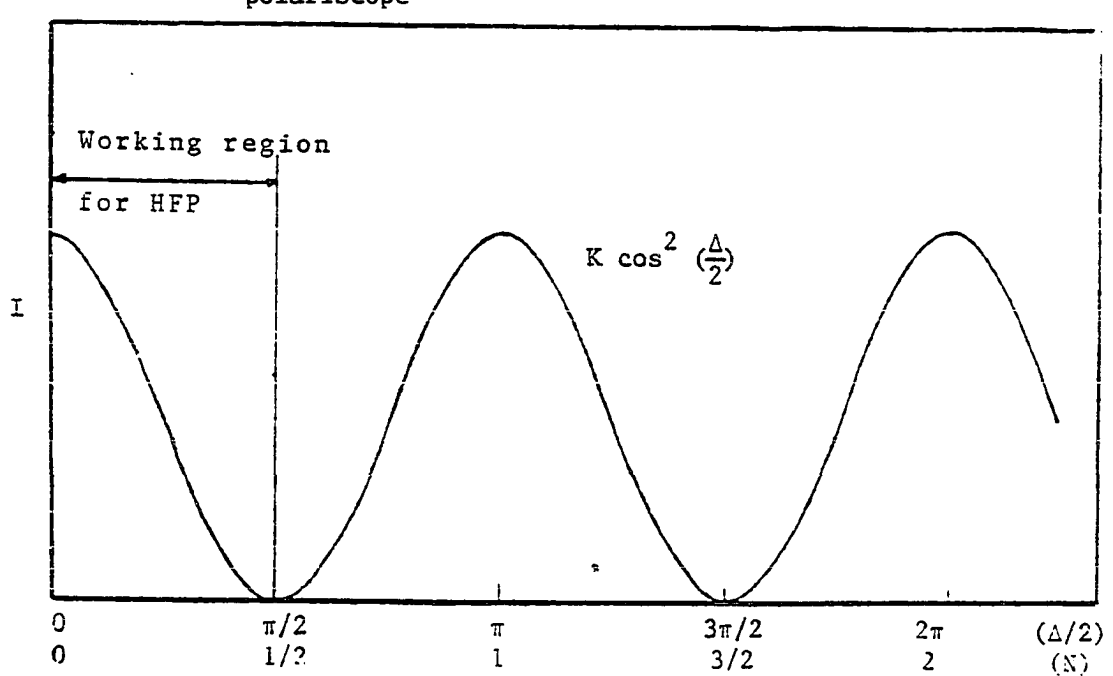


Figure 3.2. Intensity vs retardation plot for a light field circular polariscope

If a reference intensity in a dark field setup is used, the fringe order at any point, provided the maximum fringe order in the region of interest is less than .5, is

$$N = \frac{1}{\pi} \sin^{-1}\sqrt{(I/I_o)}$$

## B. EyeCom System Theory

The EyeCom System, a product of Loge/Spatial Data System Inc., is an image processing system interfaced to a LSI-11 microprocessor. Through the interface, the system allows the microprocessor full control of the hardware. The operater can select a "fast digitizing" or a "high resolution digitizing" mode. It is also possible to overlay graphic and text outputs over digitized pictures and manipulate stored images and/or live ones.

Figure 3.3 is a block diagram of the EyeCom System, as used in photoelastic studies [27]. The system consists of a regular polariscope with the video camera replacing the camera or the observer for real life measurements. It is also possible to use a frozen model in a polariscope or to view a photographic negative of a model. For the negative, only a light table is needed. In the work for this dissertation, only live models were employed. As used here, the EyeCom System includes:

. A video scanner which can use either a special vidicon television camera tube or silicon diode camera. Both cameras were used in the research reported here. The scanner divides the image into 480 lines and each line into 640 elements called pixels. This

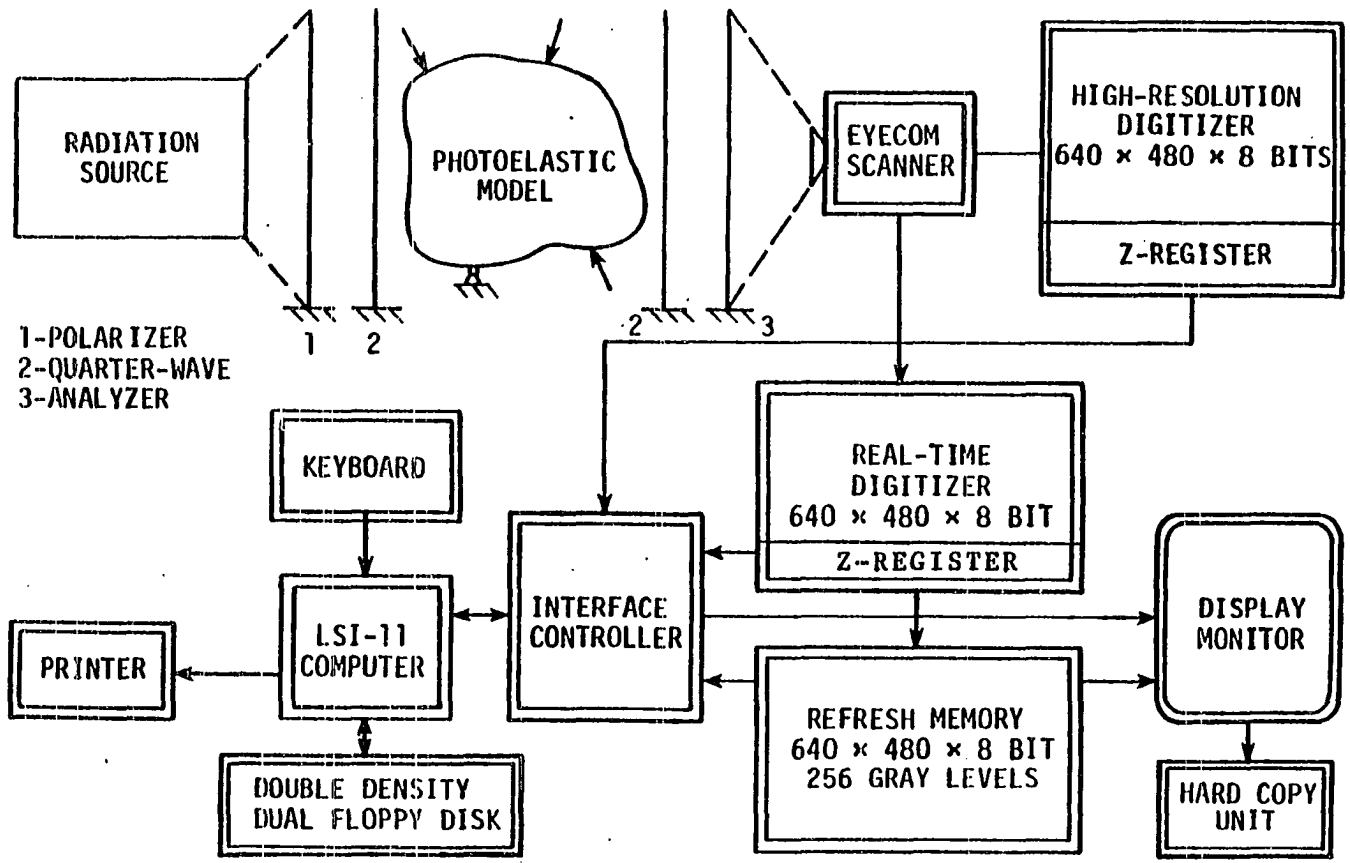


Figure 3.3. Block diagram of the EyeCom System

division produces 307,200 pixels in accordance with the American television standards. The scanning of the image is carried out in an interlace mode to reduce the flicker of the image as in normal television broadcasts. The brightness of each pixel (Z value) is converted linearly or logarithmically into an 8 bit number stored in the Z-register. The system uses a scale established by SETUP routine to expand the digitized value such that minimum Z corresponds to 0 and maximum Z corresponds to 256.

. A real-time digitizer can digitize a complete frame in 1/30 second. This fast speed require storage in a special memory called a refresh memory. The refresh memory serves as a buffer for the slower computer, which can access it at a later time.

. A high-resolution digitizer takes 2.4 seconds to digitize a whole frame. The high-resolution digitizer is used for image enhancement and for more detailed measurements, where selected finite areas of the picture are digitized. It is also used when digitizing speed is not critical and high accuracy is needed.

. Video amplifier chain performs signal correction to compensate for changes in the sensitivity across the image plane of the camera tube. It also converts the signal linearly or logarithmically to achieve the desired relationship between brightness and the digitized Z-value.

. A display monitor which has graphic capabilities. It can display graphic overlays, images from the refresh memory, text, or a live picture from the camera. It also has a special hardware display called the bit-map which reduces the continuous 256 gray levels

to a contour plot of black and white image of 64 levels of intensity. The bit map is a useful function to visualize the isochromatic fringe structure, when the overall field has very low fringe orders.

- An LSI-11 (PDP-11 family microprocessors) computer, a printer, and a hardcopy machine were used.

Graphics and picture displays are generated by scanning the refresh memory. The refresh memory stores 8 bits for each of the 640x480 pixels for the picture and graphic overlay. A second graphic display can be obtained by using the most significant bit (MSB) of the picture display to create white graphics and the 7 remaining bits to produce a 128 gray level picture.

The Z-value, that is, the digitized output from the EyeCom System, is related to the light intensity reaching the video camera, by

$$Z = K_s I^{\gamma}$$

where

Z is the digitized output from the EyeCom System;

$K_s$ is a proportionality constant which depends on the video amplifier chain;

I is the light intensity corresponding to a particular pixel;

$\gamma$ is a constant which depends on the camera used. It is about 1.0 for the vidicon camera and .65 for the silicon diode camera.

## C. Fracture Mechanics Theory

The state of stress for a plane problem (Figure 3.4) is governed by the biharmonic stress function U (also called the Airy stress function). Where

$$\sigma_{xx} = \frac{\partial^2 U}{\partial x^2} \tag{3.4a}$$

$$\sigma_{yy} = \frac{\partial^2 U}{\partial y^2} \tag{3.4b}$$

$$\sigma_{xy} = - \frac{\partial^2 U}{\partial x \partial y} \tag{3.4c}$$

With the introduction of complex variables [50-52], the biharmonic using

$$z = x + iy$$

$$z^* = x - iy$$

where

$z^*$ is the the conjugate of z

This can be reduced to

$$\frac{\partial^4 U}{\partial z^2 \partial z} * 2 = 0$$

where

$$U = z\ \Phi_1 + z^*\ \Phi_2 + \Psi_1 + \Psi_2$$

is the formal solution and $\Phi_1, \Phi_2, \Psi_1$, and $\Psi_2$ are arbitrary functions. The requirement that both stresses and displacements be real are

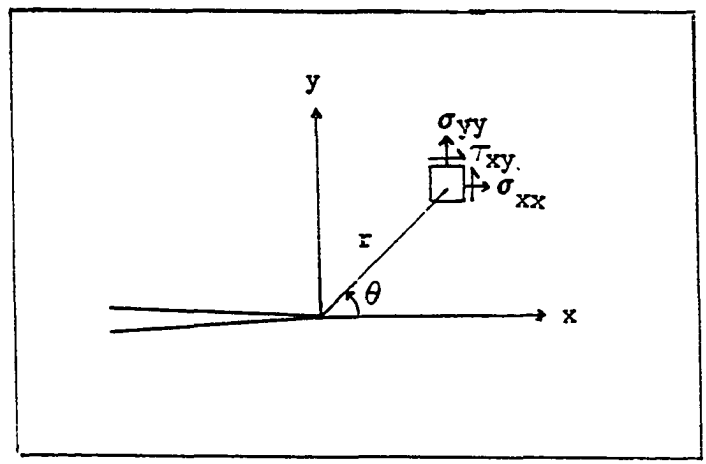


Figure 3.4. Coordinate system and stress components ahead of a crack tip

satisfied by setting

$$\Phi_2(z^*) = \Phi_1^*(z) = \Phi^*(z), \text{ and}$$
$$\Psi_1(z^*) = \Psi_2^*(z) = \Psi^*(z).$$

This is equivalent to setting

$$U = 2 \text{ Re } (z^* \Phi + \Psi) \tag{3.5}$$

where

$\Phi$ and $\Psi$ are two holomorphic functions.

Using this formal solution, it is possible to show [51,50] that the stresses can be given by

$$\sigma_x + \sigma_y = 4 \text{ Re } [\Phi'] \tag{3.6a}$$
$$\sigma_y - \sigma_x + 2i\tau_{xy} = 2 [z^* \Phi'' + \Psi'] \tag{3.6b}$$

where $\Phi'$ is $\partial\Phi/\partial z$;

$\Psi'$ is $\partial\Psi/\partial z$;

$\Psi''$ is $\partial^2\Psi/\partial z^2$.

This formal solution, which is valid for any linear elastic fracture mechanics problem, is employed to solve the stress field in the vicinity of a crack tip. Two familiar solutions are the William's solution [53] and the Westergaard approach [5]. The William's solution was developed for long cracks, thus making it suitable for edge crack problems and deep grooves. The Westergaard approach has no restrictions on the crack size, thus making it possible to develop a stress function which, in principal, would work for any case.

The Westergaard formulas are obtained by simple substitutions in Eqs. (3.6a), and (3.6b). For example, if we choose the following

$$2\,\Phi' = Z_I(z), \text{ and } 2\Psi' = -zZ_I(z),$$

this substitution gives

$$\sigma_{xx} + \sigma_{yy} = 2\ \mathrm{Re}\ Z_I;$$

$$\sigma_{yy} - \sigma_{xx} = 2y\ \mathrm{Im}\ Z_I';$$

$$\tau_{xy} = -y\mathrm{Re}\ Z_I'.$$

It is clear from this solution that, on the line y = 0;

$$\sigma_{xx} = \sigma_{yy} \text{ and } \tau_{xy} = 0.$$

This solution is a valid solution for Mode I crack problems, where the crack is subjected to an equibiaxial stress field at infinity as shown by Sih [54], Evans and Luxmoore [55], and Eftis and Liebowitz [56]. To overcome the equibiaxial stress restriction at infinity, Irwin [30] suggested the introduction of a nonsingular term $\sigma_{0x}$ in the x-direction. The modified Westergaard equations for Mode I would read:

$$\sigma_{xx} = \mathrm{Re}\ Z_I - y\ \mathrm{Im}\ Z_I' - \sigma_{ox}$$

$$\sigma_{yy} = \mathrm{Re}\ Z_I + y\ \mathrm{Im}\ Z_I'$$

$$\tau_{xy} = -\ y\ \mathrm{Re}\ Z_I'.$$

Though in many cases [13,57,58,59], this extension was adequate and it was shown to be sufficient to explain the tilt of the isochromatic fringe loops [60,61], the solution is incapable of dealing with the interaction of one crack with another or with the interactions when a subsurface crack approaches a boundary. This failure is due to the inadequacy of a single constant term, $\sigma_{0x}$, to prescribe a complex stress field such as when one crack field closes in on another stress field. It also cannot satisfy the stresses and displacements for a crack close to a straight or curved boundary. To overcome this deficiency, Sih [54] attempted to use a different substitution in Eqs. (3.6a) and (3.6b). He

introduced a constant A such that

$$\Psi'' = -z^* \Phi'' - A$$

which gives

$$\sigma_{xx} = 2 \text{ Re } \Phi' - 2y \text{ Im } \Phi'' + A$$

$$\sigma_{yy} = 2 \text{ Re } \Phi' + 2y \text{ Im } \Phi'' - A$$

$$\tau_{xy} = - 2y \text{ Re } \Phi''$$

where

A is a real constant.

This solution is no different than the previous modified Westergaard equations as shown by Eftis and Liebowitz [56], if we choose

$$2\Phi\Lambda(z) = Z_I(z) + A$$

and

$$\sigma_{0x} = 2A.$$

The greatest improvement to this solution was proposed by Sanford [60] who suggested replacing the A constant in Sih's solution by a power series. This power series would add enough arbitrariness to the solution for it to handle crack interactions with any boundary of any shape.

In the opening mode, the surface of the crack is free of shear stress and y = 0 is a plane of symmetry. This condition is satisfied by letting

$$\text{Im}(z^* \Phi'' + \Psi'') = 0.$$

Sanford [60] showed that by replacing $z^* \Phi'' + \Psi''$ by $\eta(z)$ and introducing $Z = Z_I - \eta$ in the Westergaard's solution, the stress field for Mode I is expressed by

$$\sigma_{xx} = \text{Re } Z_I - y \text{ Im } Z_I + y \text{ Im } \eta' - 2 \text{ Re } \eta \qquad (3.7a)$$

$$\sigma_{yy} = \text{Re } Z_I + y \text{ Im } Z_I - y \text{ Im } \eta' \tag{3.7b}$$

$$\tau_{xy} = - y \text{ Re } Z_I' + y \text{ Re } \eta' + \text{Im } \eta \tag{3.7c}$$

In the shearing mode (Mode II) where $\sigma_{yy} = 0$ on $y = 0$, Wang [27], Rossmanith [62], and Cottron and Lagarde [63] following Sanford's steps, showed that from Eqs. (3.6a and 3.6b)

$$\sigma_{yy} = \text{Re } ( 2 \Phi' + z^* \Phi + \Psi'' ).$$

This leads to choosing

$$\Psi'' = - (2\Phi' + z \Phi'')$$

and

$$\Phi' = Z_{II}/2i$$

where

$$i = \sqrt{(-1)};$$

$Z_I$ and $Z_{II}$ are Westergaard functions.

The last solution gives the following expressions for the stress field in Mode II

$$\sigma_{xx} = 2 \text{ Im } Z_{II} + y \text{ Re } Z_{II}' \tag{3.8a}$$

$$\sigma_{yy} = - y \text{ Re } Z_{II} \tag{3.8b}$$

$$\tau_{xy} = \text{Re } Z_{II} - y \text{ Im } Z_{II}' \tag{3.8c}$$

Though the solution satisfies the stress free condition on the crack surface, it was shown by [64] that Mode II, as described earlier, is a considerably simplified form of Eqs. (3.6a and 3.6b). Thus, we can conclude that this specialized form of Mode II is not general enough to

deal with cracks interacting with boundaries or other cracks.

In the zone very close to a crack tip, Modes I and II solutions were shown by [63] to yield Irwin's singular solution when higher orders terms are neglected. This conclusion makes the solution valid in the region very close to the crack tip. For very weak interactions, the solution could yield correct fracture parameters.

A mixed mode, generalized Westergaard solution can be obtained by superimposing the previous two solution where

$$Z_I = \sum \frac{An\ Z^{(n-1/2)}}{(n-1/2)} \qquad n = 0,\ 1,\ ..,\ N1 \tag{3.9a}$$

$$Z_{II} = \sum \frac{Bm\ Z^{(m-1/2)}}{(m-1/2)} \qquad m = 0,\ 1,\ ..,\ N2 \tag{3.9b}$$

$$\eta = \sum Cp\ Z^p \qquad p = 0,\ 1,\ ..,\ M1 \tag{3.9c}$$

For an internal crack in a finite plate, Kobayashi, Cherepy, and Kinsel [65] applied the complex variable methods developed by Muskhelishvili [51]. For a straight crack with stress free boundaries located along the x-axis and tips at x = a and -b as in Figure 3.5, the stresses are expressed by two complex functions $\Phi(z)$ and $\Psi(z)$ as

$$\sigma_{xx} + \sigma_{yy} = 2\ [\Phi(z) + \Phi^*(z)]$$

$$\sigma_{yy} - \sigma_{xx} + 2i\ \tau_{xy} = 2\ [(z^*-z)\Phi' - \Phi + \Omega^*(z)]$$

where

$$\Phi(z) = \frac{F_1(z)}{[(z-a)(z+b)]^{1/2}} + F_2(z);$$

$$\Omega(z) = \frac{F_1(z)}{[(z-a)(z+b)]^{1/2}} + F_3(z);$$

$$F_1(z) = \sum_{1}^{N1} A_n Z^n + i \sum_{1}^{N2} B_n Z^n;$$

$$F_2(z) = \sum_{1}^{M1} C_n Z^n + i \sum_{1}^{M2} D_n Z^n;$$

$i = \sqrt{(-1)}$.

Vooren [66], examining the previous solution, found that for the crack surface to be free. The $F_2$ and $F_3$ functions must be chosen such that

$$F_3(z) = - F_2(z).$$

This last conclusion was partially evident in Kobayashi's results [65]. The numerical results showed the coefficients of both $F_2$ and $F_3$ are equal within numerical accuracy limits. The lack of the negative in these results made Vooren suspicious. He concluded that it may have been a programming error.

The solution modified by Vooren was later used by Wilson [67] to study a central crack in a uniaxial tensile specimen. For the crack tip at z = a, the stress intensity factors are given by

$$K_I - i K_{II} = 2 \sqrt{2\pi} \lim_{z \to a} \sqrt{(z-a)}\ \Phi(z)$$

and for the tip at z = - b

$$K_I - i K_{II} = 2 \sqrt{2\pi} \lim_{z \to (-b)} \sqrt{(z+b)}\ \Phi(z).$$

The equations by Wilson require the solution of a set of complex equations and precise measurements of all constants to attain the correct values for $K_I$ and $K_{II}$. This problem can be overcome. Without

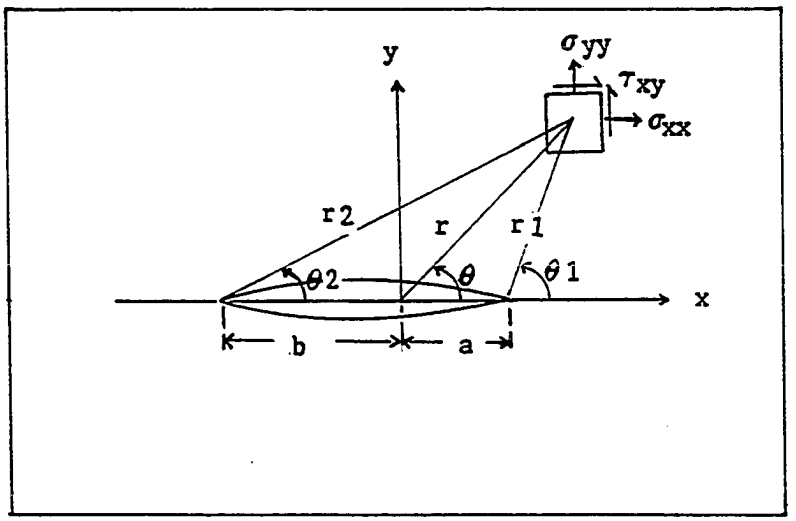


Figure 3.5. Internal crack coordinate system

loss of generality, the coordinate system can be moved to the crack tip of interest. In this case, the complex functions $\Phi(z)$ and $\Omega(z)$ are reduced to

$$\Phi(z) = \frac{\Sigma C_{1,n} Z^{n-1/2}}{\sqrt{(2a)}\sqrt{(1+z/2a)}} + \Sigma C_{2,n} Z^{n}$$

$$\Omega(z) = \frac{\Sigma C_{1,n} Z^{n-1/2}}{\sqrt{(2a)}\sqrt{(1+z/2a)}} - \Sigma C_{2,n} Z^{n}$$

where $C_{1,n} = A_n + i B_n$ and $C_{2,n} = C_n + i D_n$.

In this expression, for tip at $z = 0$, the stress intensity factors are

$$KI - i KII = 2\sqrt{2\pi} (A_0 + i B_0),$$

which require determining accurately to one single complex constant. In its present form, the solution satisfies the exact boundary conditions at the crack surface. For a more practical solution, the denominator can be expanded to yield a simpler form which is general, but requires satisfying the boundary conditions on the surface of the crack in the solution. The expanded form given by Parton and Morozov [68] is

$$\Phi(z) = \Sigma C_{1,n} Z^{n-1/2} + \Sigma C_{2,n} Z^{n}$$

$$\Omega(z) = \Sigma C_{1,n} Z^{n-1/2} - \Sigma C_{2,n} Z^{n}$$

or as used in this research

$$\bar{\Phi}(z) = \Sigma A_{n1} \bar{Z}^{n1-1/2} + i \Sigma B_{n2} \bar{Z}^{n2-1/2} + \Sigma C_{m1} Z^{m1} + i \Sigma D_{m2} Z^{m2} \qquad (3.10)$$

$$\Omega(z) = \Sigma A_{n1}\, Z^{n1-1/2} + i\Sigma B_{n2}\, Z^{n2-1/2} - \Sigma C_{m1}\, Z^{m1} - i\Sigma\, D_{m2}\, Z^{m2} \qquad (3.11)$$

where n1 =0, 1, 2,..,N1

n2 =0, 1, 2,..,N2

m1 =0, 1, 2,..,M1

m2 =0, 1, 2,..,M2

## D. Boundary Collocation Method

In this dissertation, a semi-analytical approach is used. The solution is based, in part, on boundary collocations and, in part, on half fringe photoelasticity [43]. As a crack approaches a stress free boundary, the normal stress and shear stress have to satisfy the equations

$$\sigma_{nn} = 0 \qquad (3.12)$$

$$\tau_{nt} = 0. \qquad (3.13)$$

To define the state of stress uniquely, the loading condition is introduced through the normal stress in the direction tangent to the boundary. This stress is directly related to the maximum shear at the point and for a tension specimen is given by

$$\sigma_{tt} = 2\ \tau_{max}. \qquad (3.14)$$

The shear stress, $\tau_{max}$, is, in turn, related to the fringe order at the point through the opto-elastic law

$$\tau_{max} = \frac{N\, F\sigma}{2\, h}, \tag{3.15}$$

where

N is the fringe order;

$F\sigma$ is the material fringe constant;

h is the model thickness.

Combine Eqs. (3.14) and (3.15) to get

$$\sigma_{tt} = \frac{N\, F\sigma}{h} \tag{3.16}$$

For the boundary point, the stresses can be expressed as

$$\sigma_{nn} = \sigma_{xx} \cos^2(\upsilon) + \sigma_{yy} \sin^2(\upsilon) + 2\, \tau_{xy} \sin(\upsilon) \cos(\upsilon) \tag{3.17a}$$

$$\tau_{nt} = -(\sigma_{xx} - \sigma_{yy}) \cos(2\upsilon) + \tau_{xy} \sin(2\upsilon) \tag{3.17b}$$

$$\sigma_{tt} = \sigma_{xx} \sin^2(\upsilon) + \sigma_{yy} \cos^2(\upsilon) - (\sigma_{xx} - \sigma_{yy}) \cos(2\upsilon) \tag{3.17c}$$

where

$\upsilon$ is the angle between the outward-normal to the boundary and the positive x-axis of the crack.

For KO points on the boundary, we need to solve the following linear system of equation

$$\begin{bmatrix} [A^{11}_{kn1}] & [A^{12}_{kn2}] & [A^{13}_{km1}] & [A^{14}_{km2}] \\ [A^{21}_{kn1}] & [A^{22}_{kn2}] & [A^{23}_{km1}] & [A^{24}_{km2}] \\ [A^{31}_{kn1}] & [A^{32}_{kn2}] & [A^{33}_{km1}] & [A^{34}_{km2}] \end{bmatrix} \begin{bmatrix} [A_{n1}] \\ [B_{n2}] \\ [C_{m1}] \\ [D_{m2}] \end{bmatrix} = \begin{bmatrix} [0] \\ [0] \\ [N_k] \end{bmatrix} \frac{F\sigma}{h}$$

Where

$A_{n1}$, $B_{n2}$, $C_{m1}$ and $D_{m2}$ are column arrays containing the real coefficients of the series expansions (Eqs. 3.10 and 3.11);

$N_k$ is a column array of fringe values at the boundary points in consecutive order as collected;

k is the number of points collected at the boundary;

ij superscript; i refer to Eqs. 3.17 a,b and c in order, j refer to coefficients of $A_{n1}$, $B_{n2}$, $C_{m1}$ and $D_{m2}$ in order

The calculation of stress intensity factors is reduced to the solution of an overdeterministic linear system of equations. The stress intensity factors are directly related to the coefficients of the generalized equations. The stress factors are given by

$$KI = 2\sqrt{(2\Pi)}\, A_0$$

$$KII = -2\sqrt{(2\Pi)}\, B_0$$

$$\sigma_{0x} = -4\, C_0.$$

This system of equations can be put into matrix form as

$$[Amat][x] = [Bmat].$$

Using the least squares method to this overdeterministic system of equations, we can reduce it to

$$[Amat]^T\ [Amat]\ [x] = [Amat]^T\ [Bmat]$$

or

$$[A]\ [x] = [B].$$

The last system equation is solved by using the Gauss elimination procedure to give all pertinent coefficients.

# IV. EXPERIMENTAL TECHNIQUE

## A. Model Material

PSM-1, the material used in this research, is a polycarbonate thermoplastic of excellent modeling qualities. It is an unusually tough and ductile polymer and is available commercially with good surface characteristic in large sheet sizes under the trade name Lexan in the United States [46]. The stress strain curve of this material resembles that of mild steel [69,70]. Its outstanding characteristic is a high photoelastic figure of merit Q ($Q= E/F_\sigma$), and a high sensitivity index S ($S=\sigma_{pl}/F_\sigma$) which relate to the maximum number of fringes, which can occur while the material still obeys the linear photo-optic law ($\sigma_{pl}$ = 5000 Lb/in$^2$). In addition, PSM-1 has little creep at room temperature and is relatively free of time-edge effects.

Residual bifringence may be produced in the extrusion process of large sheets of this material. Annealing can remove the residual bifringence, but the process is laborious. Commercially annealed sheets are sold under the trade name PSM-1. Plastically introduced bifringence, in contrast, is permanent and can only be removed by diligently filing away the plastically deformed region. Since the material is thermoplastic, it can easily deform and flow from heat generated by a cutting tool during model manufacturing.

To prevent softening, cutting and routing are done in a cooling bath of kerosene or water. When trying to produce narrow slits, side milling is impractical. Sawing, followed by careful hand filing, is

Table 4.1. Optical and mechanical properties of PSM-1. Dally and Riley [46]

| Property | Value |
|---|---|
| Time-edge effect | Very small |
| Creep | Very small |
| Machinability | difficult |
| Modulus of elasticity E; | |
| $Lb/in^2$ | 360,000 |
| MPa | 2480 |
| Poisson's ratio $\nu$ | 0.38 |
| Proportional limit $\sigma_{pl}$; | |
| $Lb/in^2$ | 5000 |
| MPa | 34.5 |
| Stress fringe value $F_\sigma$; | |
| Lb/in | 40.0 |
| KN/m | 7.0 |
| Strain fringe value $F_\varepsilon$; | |
| in | 0.00015 |
| mm | 0.0038 |
| Figure of merit Q; | |
| 1/in | 9000 |
| 1/mm | 354 |
| Sensitivity index S; | |
| 1/in | 125 |
| 1/mm | 4.92 |

often required to produce satisfactory crack surfaces. Table 4.1 is a summary of PSM-1 material properties.

## B. Test Specimen

Test models were fabricated from PSM-1. The models were rectangular plates, 2 inches wide and 10 inches long. The thickness of the sheet used to make the models was 0.13 inches. The crack was artificially introduced by cutting with a fine jewelry saw to produce a fine through thickness slit of 0.006 inches wide and 0.8 inches long. This slit simulates an internal crack of length $2a = 0.8$ inches with a crack root radius of $\rho = 0.003$ inches. All necessary precautions, like cutting under a kerosene bath to prevent heating of the model, were taken. Figure 4.1 shows a typical model and Table 4.2 lists all models used in this research.

## C. Experimental Procedure

The model of Figure 4.1 is mounted in a loading frame with its edges perfectly aligned with the direction of applied forces. Once the model is aligned properly, it is eased into the circular polariscope table where a TV camera looks on. The lens aperture of the camera is then adjusted for the correct amount of light for no saturation (flooding) at either the black or white region of the model. It is focused to show the particular area of interest in the model. This area of interest is the edge boundary near the crack tip. It is aligned to

Table 4.2. Crack angle β vs d/a the shortest distance of tip from the boundary to the crack length. All Models are made of PSM-1, 2" wide 10" long and .13" thick. a is .4"

| Model | β (Deg.) | d/a |
|---|---|---|
| A | 30 | .25 |
| B | 30 | .375 |
| C | 30 | .50 |
| D | 30 | .625 |
| E | 30 | .75 |
| F | 30 | 1.00 |
| G | 60 | .25 |
| H | 90 | .25 |

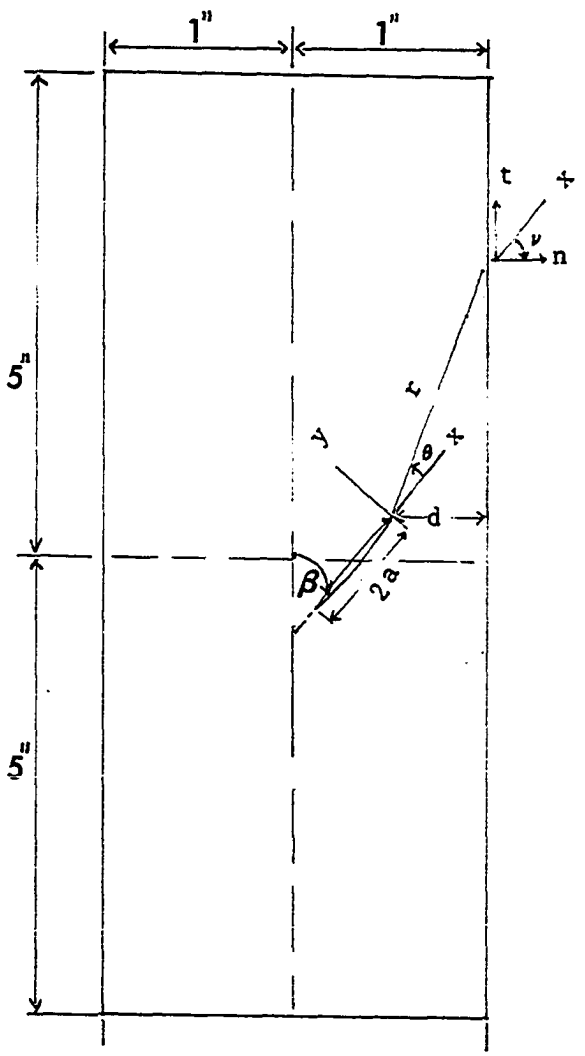


Figure 4.1. Model used and local coordinate system

be horizontally parallel to the center line of the screen and the crack tip is in the center. Once initial adjustment on the model and camera are completed, it is necessary to calibrate the system.

## D. Calibration of the EyCom System

### 1. Internal self calibration

The EyCom System circuitry requires some time to stablize after starting from cold. The operator needs to check if the system has reached a stable state by running a hardware routine called "SETUP." SETUP gives a number which indicates if the system is ready for image processing. Two other registers "Zero" and "Range" are controlled by Setup. Zero register references the light intensity to which a digitized Z-value of zero is assigned. Range, which has a value 0-63, gives the scale which the Z-value requires, such that Zmin to Zmax span 256 gray levels. The program SETUP (Figure 4.2) asks the operater to cover the lens and it scans the video image plane once, while the camera lens is capped to establish the condition number. Second, we asked the program to adjust the zero register and range. SETUP prompts to move the cursor to the darkest spot on the screen and hit the back space key, <BS>. This establishes the minimum Z-value, Zmin. Last, the program prompts to move the cursor to the lightest spot in the image once and <BS> is hit for SETUP to establish the maximum Z-value Zmax. The internal calibration is repeated at the start of every new experiment to insure proper adjustment of the system. Starting from cold, the condition number indicates whether the system is ready for data

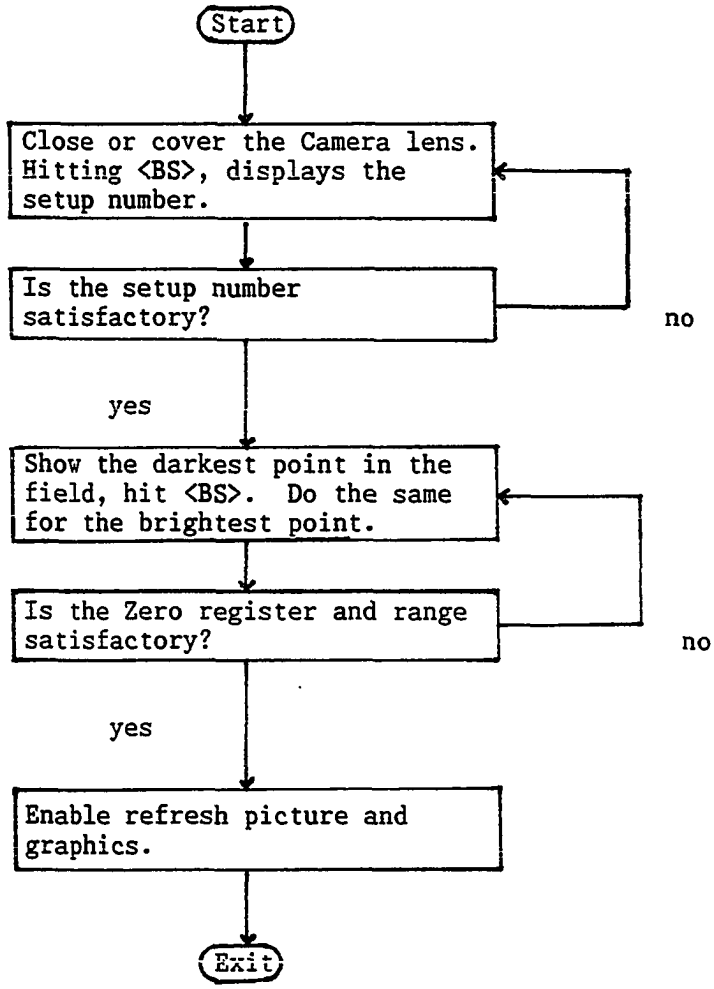


Figure 4.2. Block Diagram of program SETUP

collection or more time is needed for the internal circuitry to stablize. The zero register and the range, on the other hand, establish the proper scale for the digitized output Z-value in the region of interest.

## 2. External Calibration by Program CAL2A [72]

External calibration of the EyeCom System is the second important step in the preparation for data collection. To understand the logic behind this step, it is necessary to reexamine the relationship between the light intensity, I, striking the camera image plane and the digitized, Z, output of the system. It is shown in the EyeCom II handbook [71] that

$$Z = K\, I^{\gamma} \tag{4.1}$$

or on a log scale by

$$\text{Log } Z = \text{Log } K + \gamma \log I \tag{4.2}$$

where

Z is the digitized output of each pixel;

I is the light intensity striking the pixel;

$\gamma$ is the slope of the log-log response curve of the camera;

K is proportionality constant.

At maximum intensity, Imax, the digitized output Zmax is also related by

$$Zmax = K\, I^{\gamma}max \tag{4.3}$$

To eliminate the proportionality constant, we divide Eq. (4.1) by Eq. (4.3) which simplifies the relationship to

$$Z/Zmax = (I/Imax)^{\gamma} \tag{4.4}$$

for dark field setup,

$$I = I_o \sin^2(n\pi) \tag{4.5}$$

where

n is fringe order;

$I_o$ is reference intensity.

Substituting Eq. (4.5) into Eq. (4.4) and simplifying, we get

$$Z/Zmax = \sin^{2\gamma}(n\pi)$$

or in a log scale as

$$\log(Z/Zmax) = 2\gamma \log(\sin(n\pi)). \tag{4.6}$$

A plot of the previous equation of log (Z/Zmax) vs log(sin(nπ) should yield a straight line which passes through the origin. In practice, it is observed that this line crosses the axis at some location other than the origin. This discrepancy is attributed to electrical and optical noise in the system and can be accounted for by the addition of a constant term log(B). The corrected form is

$$\log(Z/Zmax) = 2\gamma \log(\sin(n\pi) + \log(B) \tag{4.7}$$

or

$$n = (1/\pi)\arcsin[(Z/(B\ Zmax))^{1/2\gamma}]. \tag{4.8}$$

To estimate fringe orders automatically, it is necessary to obtain the values for $\gamma$, B, and Zmax. Program CAL2A [72], based on Eq. (4.7), is used to calibrate the EyeCom System.

While the specimen is under no load condition, the fringe order, n, can be related, from the Tardy Eq. (3.3) to the analyzer angle, $\alpha$, measured from crossed analyzer position. The fringe order is

$$n = \alpha/\pi.$$

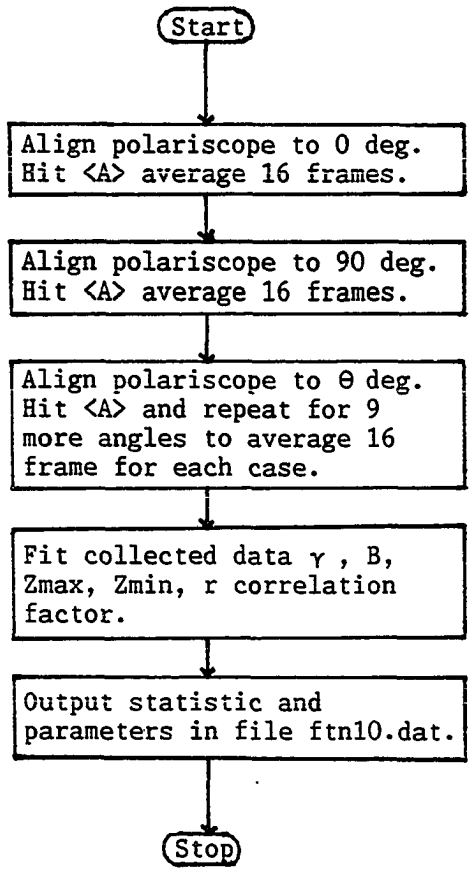


4.3. A block diagram of Program CAL2A

To obtain $\gamma$, B, and Zmax, the program collects Z and n information about ten analyzer angles such as, for example 0, 9, 18, 27, 36, 45, 54, 63, 72, 81, and 90 deg. A best fit using least squares method is applied to Eq. (4.7). A correlation factor to determine goodness of fit and percent error are also calculated for each data point. At the end of the analysis, CAL2A outputs its results to the screen and then stores it in file, ftn10.dat, for later use. Figure 4.3 is a block diagram for CAL2A operation.

## E. Data Collection Method

To collect data, the analyzer is set in the dark field position. Then, the model is subjected to a uniaxial tensile force. The applied load is kept low enough so that the fringe order does not exceed one-half fringe order at the boundary where data collection is performed.

### 1. Data collection by program GBDAT

Program GBDAT (Figure 4.4) is the main data collection routine. It was written for this research. At the beginning, the program asks the operater if a new image is to be digitized and stored in the refresh memory. The operater may proceed by taking a new image or work with a previously stored one. The image stored is the average of 16 sequentially-collected frames to eliminate the time varying random electronic or optical noise. The 16 frame averaging is used in all cases reported herein to perform the complete image aquisition on the

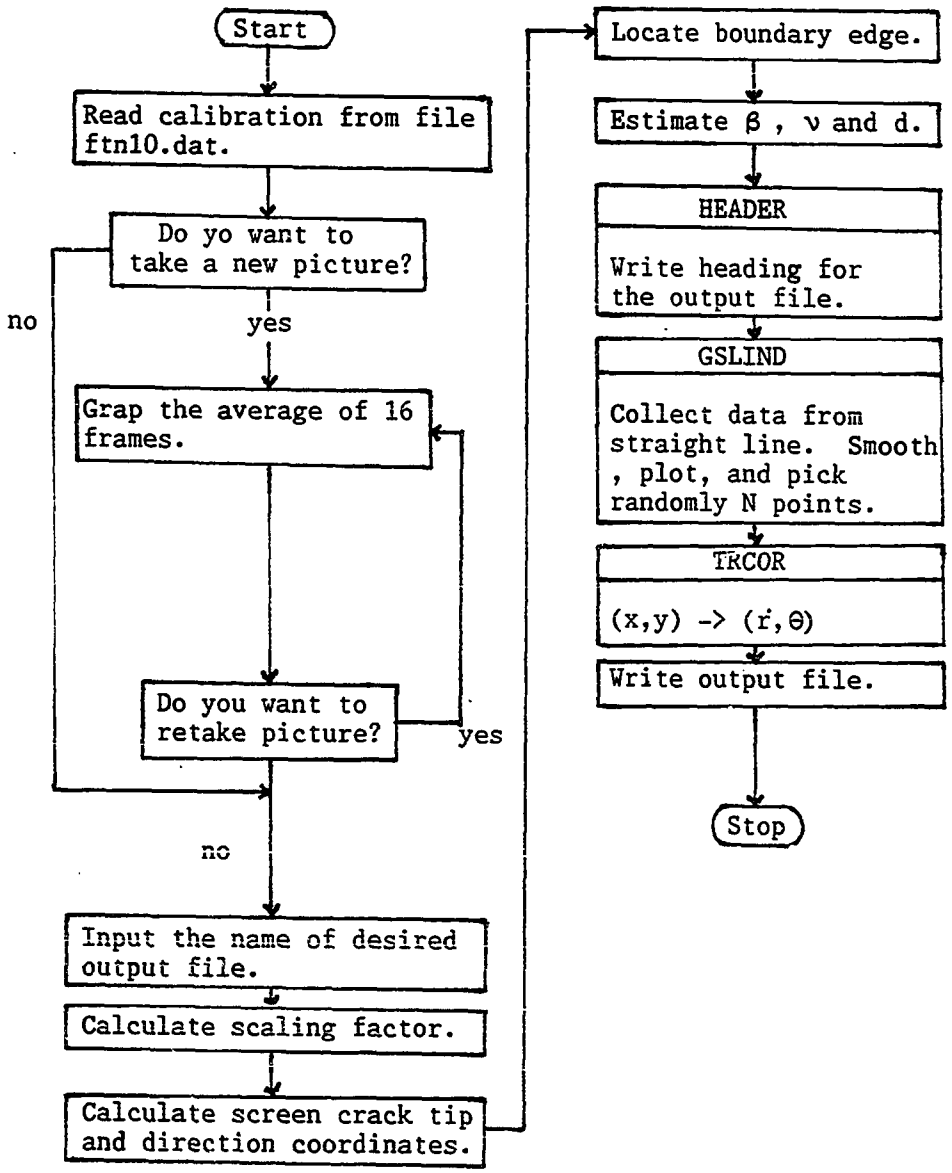


Figure 4.4. Block diagram of program GBDAT

EyeCom System. For point-by-point collection, any number of averaging can be used to eliminate noise of random character. Operating on the stored image removes problems related to load relaxation, temperature changes, and drifting in the electronics from affecting data collection. The stored image is further immune from creep that may be present in some model materials.

This was not a problem with PSM-1, our model material, under the low loads used here and at room temperature.

On the live image, the operator inserts a grid or ruler to establish a geometric scaling factor. Correct picture-to-model dimensions are calculated by moving the cursor to one point on the scale and hitting the backspace key <BS> on the terminal. The procedure is then repeated for another point, after which the true distance between the two points is entered from the terminal. The program then calculates the scaling factor to be used later.

The normal procedure was to "grab" the image from the live model, i.e., take the 16 frame average, and store it in memory. Subsequent analysis was then preformed on the stored image.

To locate precisely the edge of the model where data collection is intended, GBDAT displays the stored image. The operator then moves the cursor to one side of the edge and hits <BS>, moves the cursor to the other side of the boundary edge and does the same. The program, GBDAT, then collects and plots light intensity across the boundary and along the line formed by these two points. The plot (Figure 4.5) shows a a line crossing the boundary where the light intensities are collected. The light intensities are plotted, relative to a horizontal base line.

Figure 4.5. A Light intensity plot across the boundary edge to recognize one point exactly on the boundary line. The line crossing the edge is where intensity is collected while the horizontal line is an arbitrary base line for the plot.

The sudden jump in light intensity marks the point where the inclined line crosses the edge. The sudden jump is caused by the sudden change in transmittability of light from air to the PSM-1 material. The point is determined by moving the cursor to the point on the plot where the jump occurred and hitting <BS>. GBDAT then calculates the correct coordinate of the point and shows it on the boundary for confirmation. If the confirmation, for some reason, is not satisfactory the calculation can be repeated for this point. A second point is needed to define a straight boundary, which can be found by repeating the previous step.

The crack tip coordinate (Figure 4.1) is established by calculating two points on the crack line. The cursor is moved to the first point, the crack tip, and the <BS> key is hit. This retrieves the screen coordinates of the crack tip (IXT,IYT). In a similar manner, the screen coordinates of a second point (IXD,IYD) are obtained. The second point is chosen on the negative x-axis of the crack. From the coordinates of the previous two points, GBDAT calculates the cosine ratios needed to convert screen coordinates to local crack tip coordinates. From the coordinates of the two points on the boundary edge and the coordinates of the two points on the crack line, the crack angle $\beta$, with respect to the loading direction, the shortest distance to boundary, is then calculated by program GBDAT.

Program GBDAT opens and reads the calibration data from file ftn10.dat generated by CAL2A. The data are used to convert light intensity to fringe orders automatically in HFP setup.

To collect data from the boundary, the experimenter places the

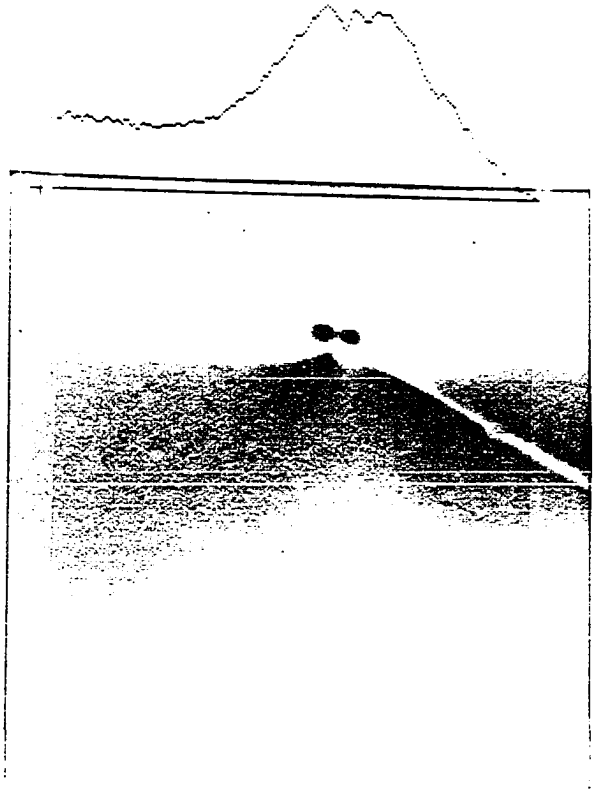

Figure 4.6. Light intensity plot a long a line from which data are collected after smoothed

cursor at the first point next to the boundary and hits <BS>. He then points to the second point next to the boundary and hits <BS> again. The program requests the number of points to be collected (less than 70) and the choice for sign of the fringe orders. The intensity along the defined line is collected by GBDAT. Then, GBDAT makes a call to the IMLIB library where the subroutine SMOOTH is resident [72]. SMOOTH preforms a sliding average operation which smooths the collected light intensities. The smoothing removes any sharp spikes in the plot which could be present due to scratches or residual stresses. The points of data are chosen randomly from this line and their screen coordinates are stored.

After data from the boundary are collected, GBDAT transforms the data screen coordinates to the crack tip coordinates and scales them to the proper dimensions.

Finally, GBDAT asks for heading information about the experiment and the name of the output file. It records the date and time of the experiment, and generates an output file for this run. The experimenter then either starts another collection cycle or the program terminates.

## 2. Data Collection by Program RECSCA [73]

Program RECSCA is used to collect both the light intensity and the screen coordinates of a rectangular grid. The grid can be as large as 50x50 grid points and the light intensity is averaged over a minimum 3x3 pixels. The light intensities (or fringe orders) collected by this routine can be plotted by the program SIMCON. The contour plot produced by SIMCON can serve as a reference of the actual fringe pattern to which

back plots of calculated fringe values are compared. This allows confirmation of the results from the boundary collocation method of extracting $K_I$ and $K_{II}$ from data collected only along the boundaries. By comparing the resultant back plot of the equivalent maximum shear stress field (fringe field) with actual fringes in the interior region where data were not collected, the correction of the experimentally determined SIFs can be checked. The coordinates of the grid points and their light intensities are stored in a data file, which can be accessed later by other subroutines for further analysis. RECSCA is also capable of converting light intensities to fringe orders. To convert light intensities to fringe orders, the calibration data in file ftn10.dat are read by RECSCA and a second file containing the screen coordinates and fringe values are stored. Figure 4.7 is a block diagram showing the RECSCA data collection procedure.

### F. Stress Intensity Factors Calculation by Program SIFBBC

Based on the boundary collection scheme and the generalized solution for an interior crack, SIFBBC (Figure 4.8) calculates the stress intensity factors for a mixed mode problem. The number of coefficients are variable and only limited by the computer memory. The program is user friendly and prompts the user with the questions to answer. To start calculation, we enter the number of terms in the series expansion of Eqs. (3.10) and (3.11). The number of terms were kept the same for both series. Then, SIFBBC asks for the name of the data file generated by GBDAT which contains the boundary points. After

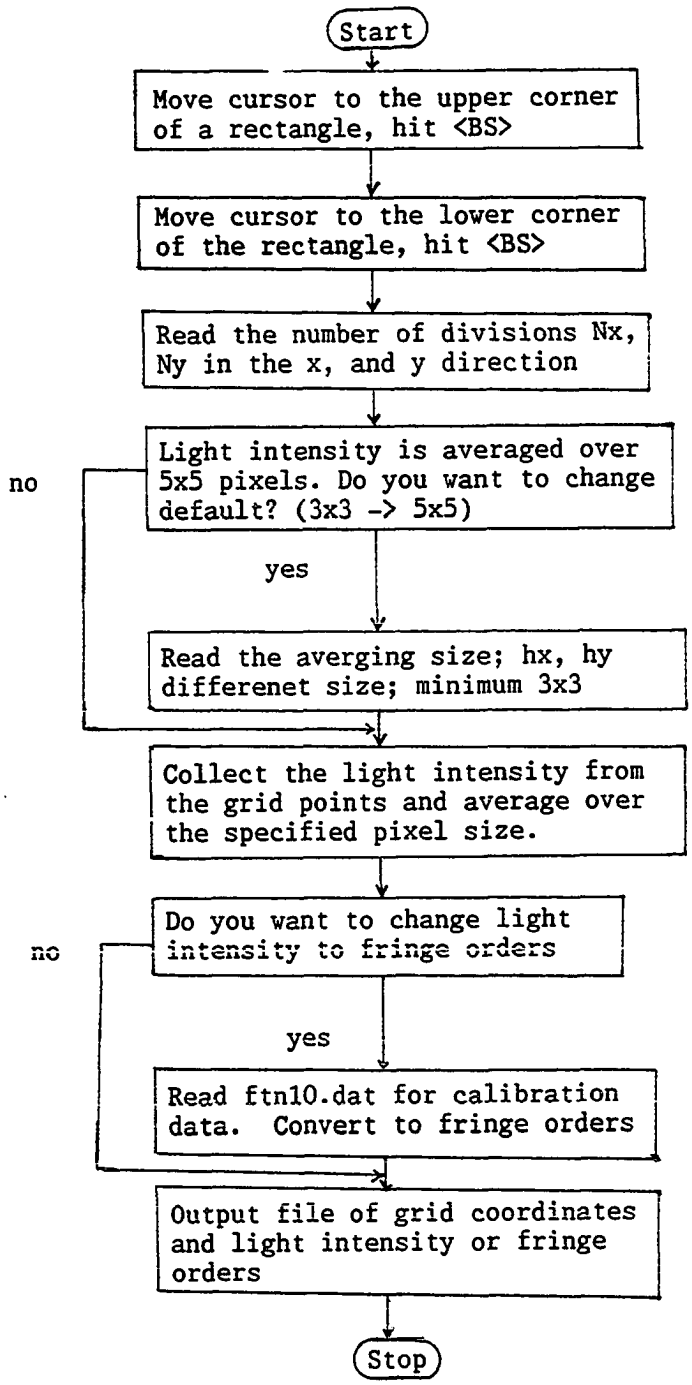


Figure 4.7. Data collection by RECSCA program

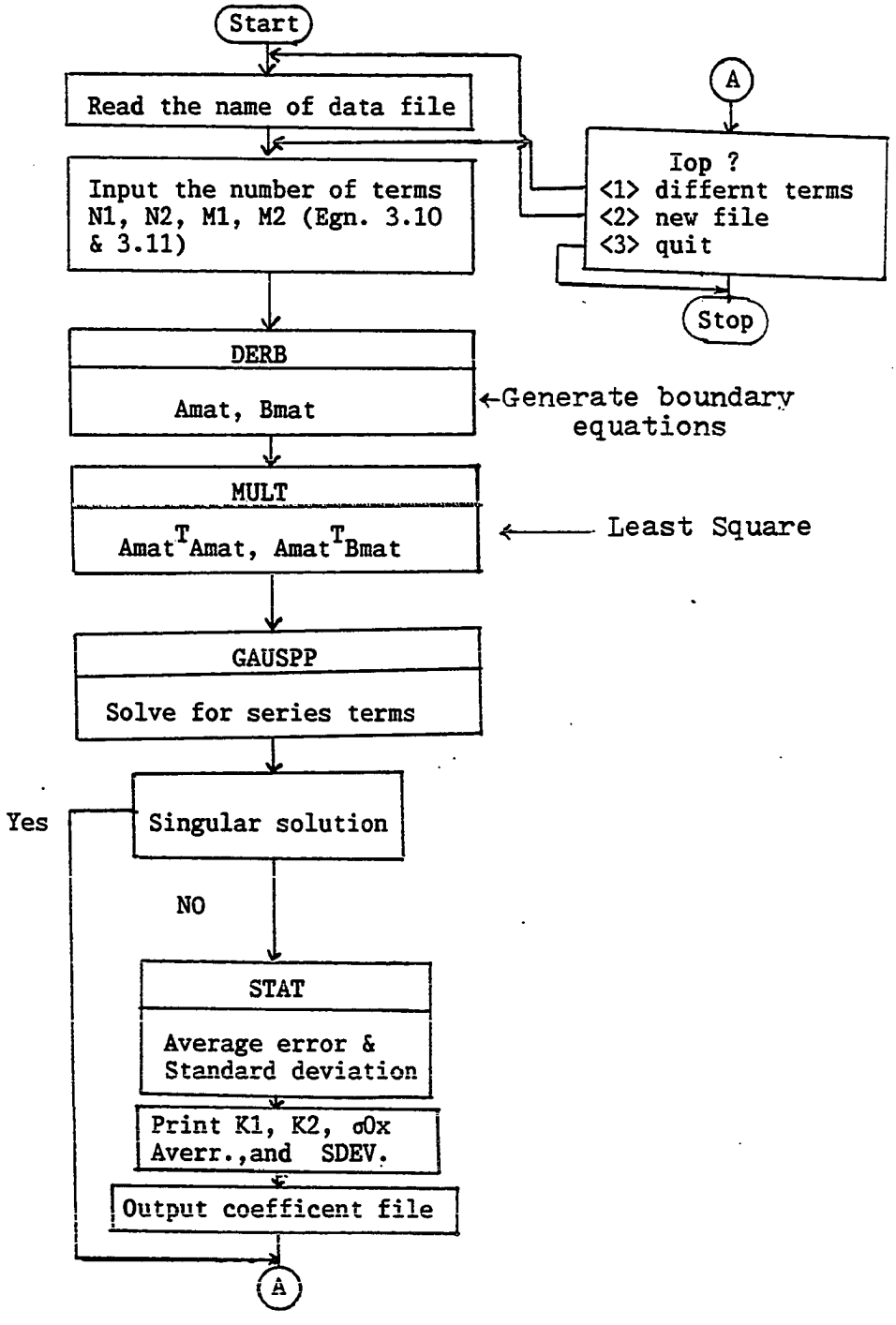


Figure 4.8. Block diagram of SIFBBC program

the program finishes calculation of the series coefficients, we direct the program to print the stress intensity factors, print all coefficients and/or output a file of the coefficient calculated by answering yes or no to the proper questions, and giving name to the output data file.

After one calculation, another calculation for a different number of terms or for new data files can be repeated as many times as necessary to obtain a good back plot. To determine the best number of coefficients which represents a particular experiment, it is necessary to back plot the results obtained by the SIFBCC program

## G. Back Plot Fringe Data Generation by Program CMFR

The fringe orders are calculated by the CMFR (Figure 4.9) routine. To calculate fringes, the CMFR program reads the material properties, the crack tip coordinates, and the direction of the crack from the data files generated by GBDAT routine. The program also reads two other files, the data file generated by RECSCA which contains the screen coordinates for the interior points, and the data file generated by SIFBBC which contains the coefficients for the series expansion of the stress functions used in the solution. For each point of the grid generated by RECSCA, the program converts the screen coordinates to the crack tip coordinates and then estimates the fringe order at this point. After the fringe orders are calculated for all data points, the program outputs a data file of screen coordinates and fringe orders of these points for a plotting subroutine.

## H. Back Plot Generation by Program SIMCON [73]

The program SIMCON uses interpolation schemes to generate a contour plot for any function, as long as the values of the function and the screen coordinates of the grid points are given. To verify the solution, two data files are plotted by this program. The data file generated by RECSCA contains either the actual intensities or the equivalent fringe orders. Plotting the fringe file provides the reference of isochromatic fringes to which we compare back plots in the interior region. SIMCON is then used to back plot the data files created by the program CMFR and contains the calculated fringe orders at the grid points created by program RECSCA. A back plot can be overlaid over the actual isochromatic fringes on the screen while doing the initial analysis. Later, we compared the back plot to the contour plot. If the calculated fringes did not match the shape and direction of the actual fringes, results were rejected on the basis of the back plot. If generating a satisfactory plot was not achieved, the values for the stress intensity factors were taken as the solution converged to a value changed little for different combination of terms. The absolute average error and standard of deviation of error between the fringe orders estimated and the actual ones collected at the boundary was minimum. The number of terms which gave the smallest mean error and smallest standard of deviation was considered the best fit. The data of the best fit were then plotted.

The back plot can be overlaid on the screen over the bit map picture or later as a second means of verification. The bit map, a

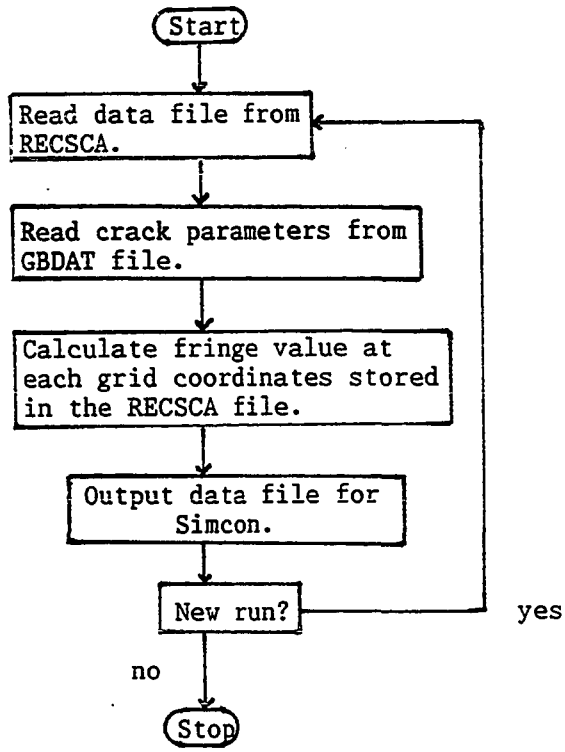


Figure 4.9. Block Diagram of CMFR Program

hardware function of the EyeCom System, automatically generates a picture where all pixels with the third least significant bit (LSB) set are turned on (white) and all pixels with the third LSB not set are turned off (black). The bit map is, thus, an intensity contour plot of equal intensity steps. The bit map has the effect of replacing a picture with 256 levels of gray to 64 levels.

In addition to comparing plots, a boundary element program [74] was run. The boundary element method 'BEM' results are compared with our method and the results are plotted.

# V. RESULTS AND DISCUSSIONS

The method of boundary collocation described earlier in section (III.D) combined with half fringe photoelasticity were administered to eight models listed in Table 4.2. The models were all made of PSM-1, 2.0 inches wide, 10.0 inches long, and .13 inches thick and have cracks of length (2a=.8 inches). Figures 5.1 and 5.2 show the contour map and the best back plot generated for the model's H and C. The other models show weak back plot match. Since we are comparing back plots of isochromatic loops in the far field, this requires accurate determination of the higher order nonsingular terms. The higher order terms did not seem to converge in general. On the other hand, the lower order terms converged more easily, which explains the good agreement with boundary element method results despite the lack of confirmation from the back plot in most cases. The stress intensity factors for Modes I and II are compared for different terms of the series expansion with BEM. The results for the two models are shown in Figures 5.3 and 5.4. Table 5.1 is a numerical comparison between boundary collocation (Exp.) and the best results with boundary element method (BEM). The experimental results shown in Table 5.1 are the nondimensional values for $K_I$ and $K_{II}$. The values are nondimensionalized with respect to $K_0$ ($\sigma\sqrt{\pi a}$). For d/a < .4, only one term was included from the first series. The second series order were increased to obtain the minimum absolute error and the smallest standard of deviation. For d/a > .4, the imaginary part of the second series were ignored. The first three coefficients were increased to obtain the smallest error. For d/a > .4,

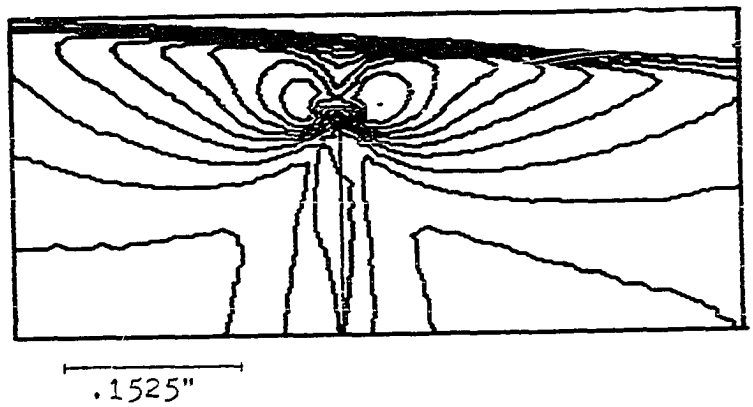


a) contour map for model h

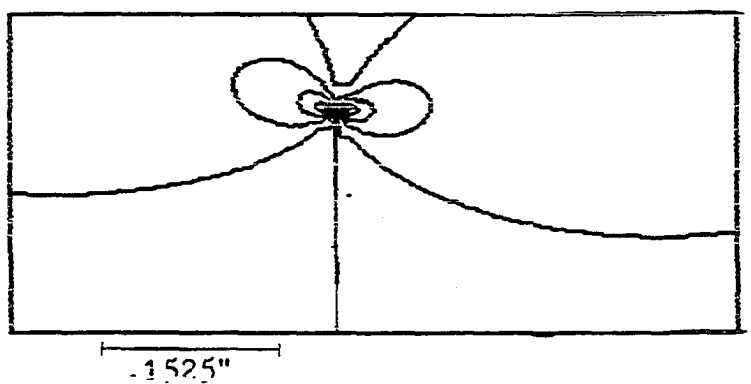


b) back plot for model h

Figure 5.1. a contour map and a back plot for model h

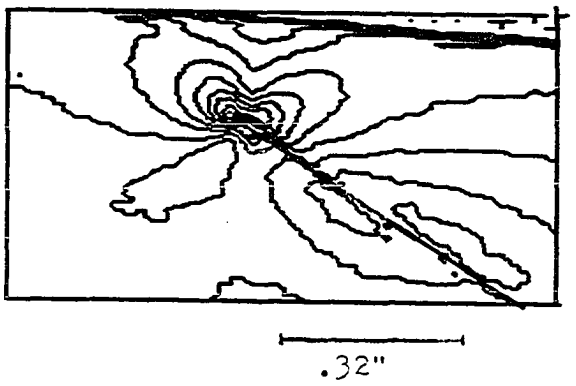


a) contour map for model c

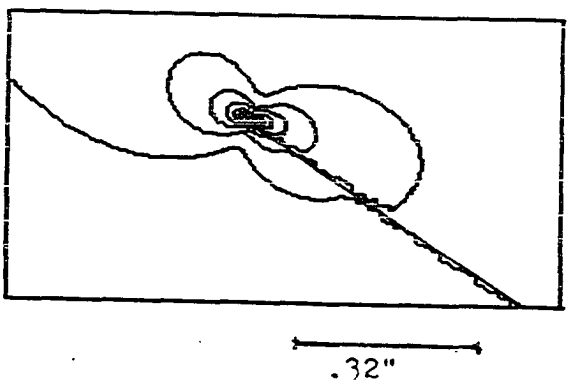


b) back plot for model c

Figure 5.2. a contour map and a back plot for model C

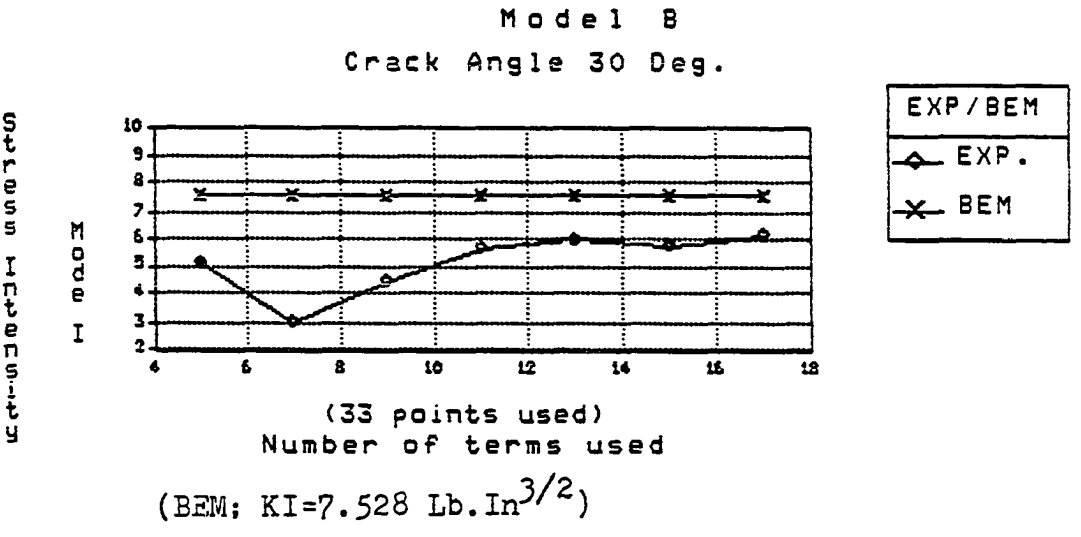


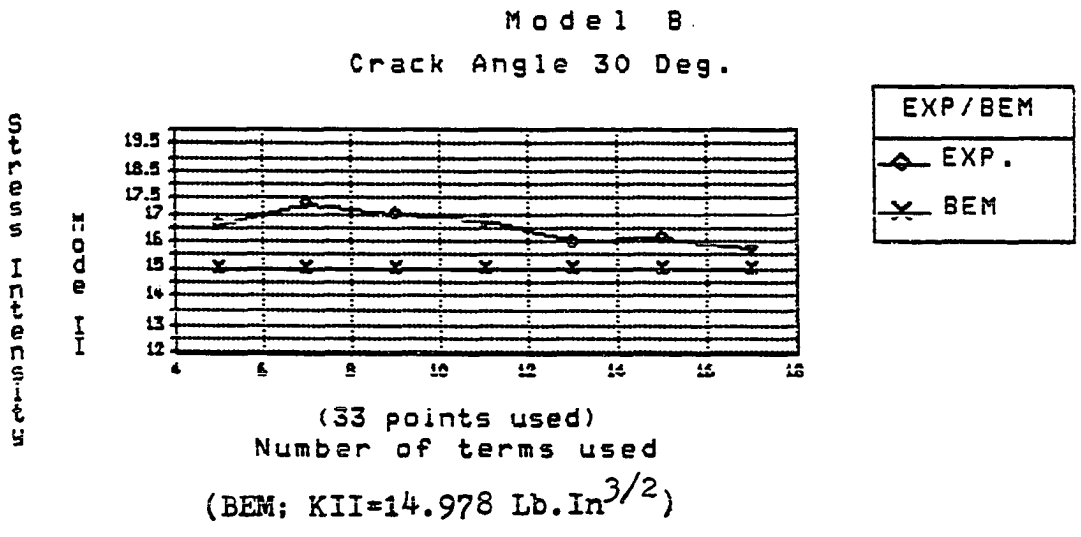


Figure 5.3. SIFs (Exp.) vs number of terms and BEM for model B

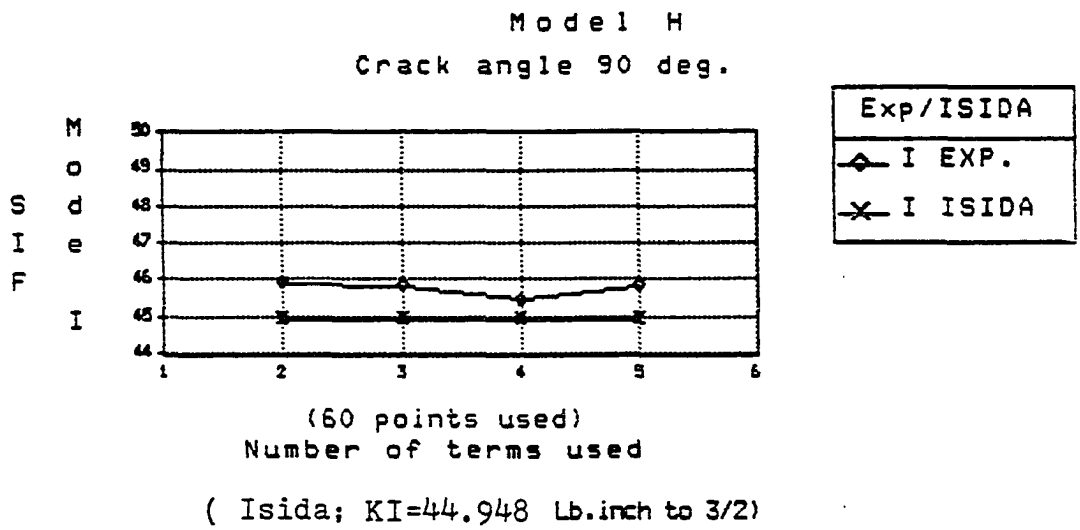


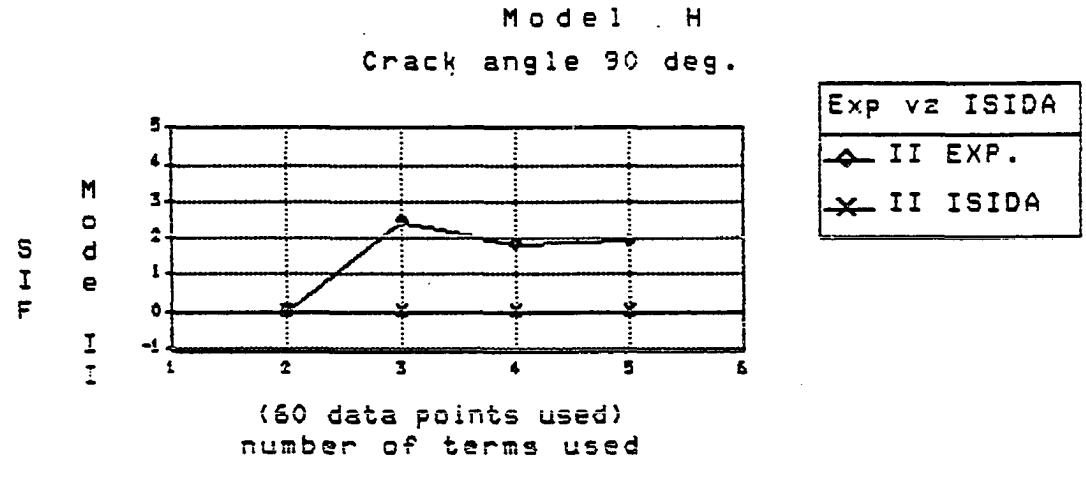


Figure 5.4. SIFs (Exp.) vs number of terms and Isida [75] for model H

Table 5.1. Nondimensional stress intensity factors for the eight models. $K_{I,II}/K0$ where $K0 = \sigma\sqrt{(\pi a)}$; $\sigma$ far field stress and a the crack length. For model H, Isida $K_I/K0=1.738$

| D/A | $K_I$-BEM | $K_I$-EXP | % | $K_{II}$-BEM | $K_{II}$-EXP | % | Model | Deg. |
|---|---|---|---|---|---|---|---|---|
| .250 | .284 | .354 | 24.6 | .619 | .449 | 27.5 | A | 30 |
| .375 | .291 | .238 | 18.2 | .579 | .609 | 5.2 | B | 30 |
| .500 | .289 | .275 | 4.8 | .553 | .497 | 10.1 | C | 30 |
| .625 | .288 | .324 | 12.5 | .533 | .633 | 18.8 | D | 30 |
| .750 | .287 | .275 | 4.2 | .518 | .497 | 4.1 | E | 30 |
| 1.000 | .287 | .332 | 15.7 | .497 | .392 | 21.1 | F | 30 |
| .25 | 1.229 | 1.182 | 3.82 | .649 | .545 | 16. | G | 60 |
| .250 | 1.643 | 1.756 | 6.9 | .001 | .07 | | H | 90 |

9 terms (A0...A2, B0...B2, C0...C2) seems sufficient to give good results.

The two methods are in good agreement for $K_I$ (4%-13%) for .4 < d/a < 1.0 and an angle $\beta$ of 30 degree. For $K_{II}$, there is lack of agreement (10-21%) for the same range and for $\beta$ of 30 degree. For $\beta$ equal to 90 degrees, the model is in pure Mode I. For Mode I, Isida's [75] analytical results for this model give $K_I/K_0$= 1.738, which is 1% lower than the boundary collocation results and 5.5% higher than the BEM method. The $K_I$ estimated for model H (90 degrees) agrees very well with the analytic results (1%) as well with the BEM (7%). The back plot for this model also shows a good match with the contour map. Because of symmetry in model H, most of the higher order terms do not affect the solution, this led to faster convergence of the solution.

In general, it was found that if we allowed the minimum fringe order to enter into the solution (more than .05 for model B), this tended to give a better convergence and to increase the number of terms for which the solution converged (17 terms for B). This imposed conditions on the fringe order collected from the boundary produced one order of magnitude less in the average absolute error and standard deviation and seemed to improve the results. This observation indicates numerical instability, due to severe approximations in the Gaussian elimination procedure used. This problem may be overcome by using double precision or weighing the terms to produce a more stable matrix to permit more accurate estimation of the higher order terms.

The boundary collocation has demonstrated reasonably to estimate the fracture parameters, $K_I$ and $K_{II}$, in the range .4 < d/a < 1.0. For

d/a > 1.0, the stress field is hardly influenced by the presence of the crack that estimating the fracture parameters, $K_I$ and $K_{II}$, is not possible. For d/a < .4 where strong interaction should be present, the method fails to estimate these parameters. One way to improve the results in the region d/a < .4 may be through forcing the boundary conditions along the crack surfaces. The boundary conditions at the crack surfaces can be enforced either by applying the boundary conditions on finite number of points on the crack surfaces or using the unexpanded form which enforces the boundary conditions at the crack surfaces exactly. When the unexpanded form is used, it shows better results for d/a < .4 for the models listed in Table 4.2 earlier.

### A. Effects of Crack Tip Distance to Boundary on the SIFs

The crack tip distance from the boundary has significant influence on the values of $K_I$ and $K_{II}$. Figure 5.5 presents the stress intensity factors for the six models for a constant $\beta$ of 30 degrees and different (d/a) dimension of the ligament, i.e., of the distance from the crack tip to the boundary. The results indicate strong interactions when the ratio (d/a) (crack tip distance to crack length ratio) is smaller than .4. The results show a trend of increasing SIFs as the ratio (d/a) is decreased for Mode II, while for Mode I the values change little. This conclusion is in agreement with the numerical results obtained by the boundary element method (BEM), which predicts almost a constant value for $K_I$ and increasing value for $K_{II}$ as the ratio (d/a) is decreased.

BEM predicts little change in the value of $K_I$ in the range .25 <

Stress Intensity Factor

Mode I

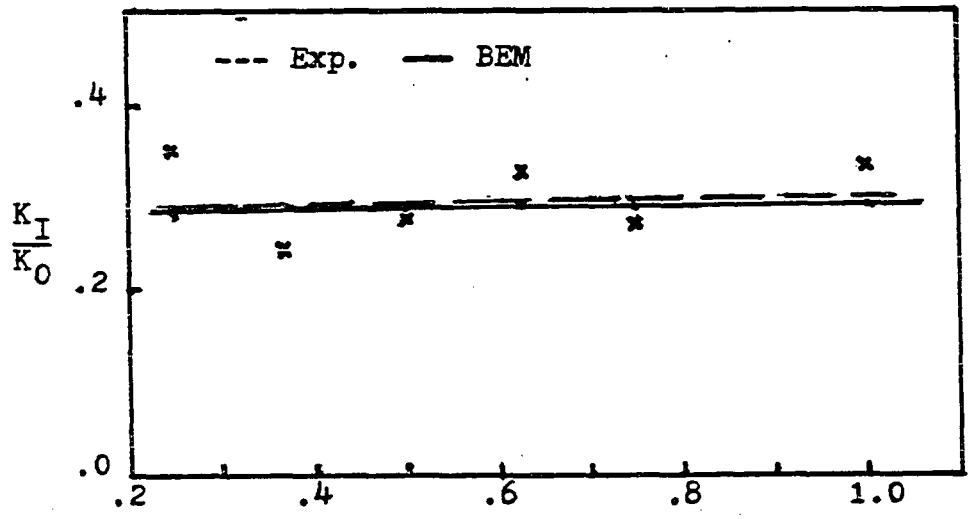


Boundary distance/crack length (d/a)

Stress Intensity Factor

Mode II

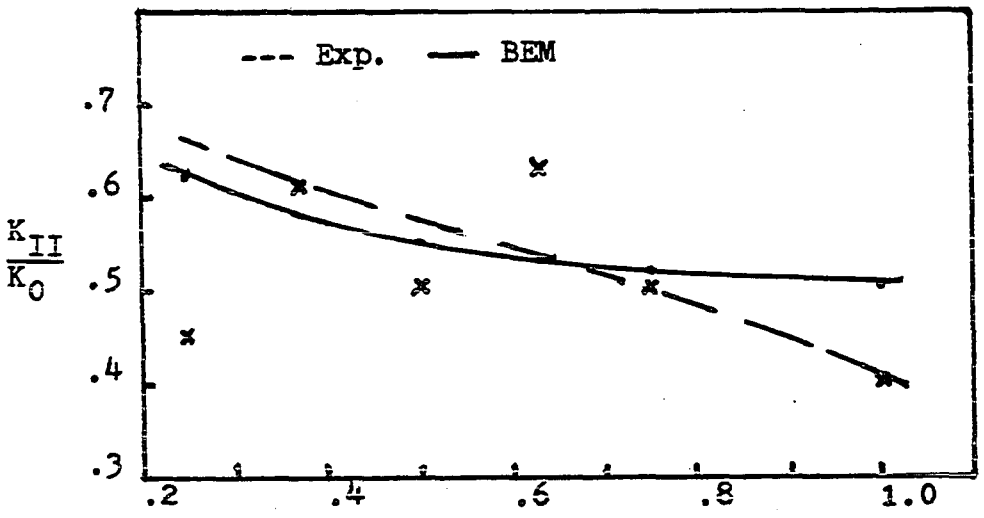


Boundary distance/crack length (d/a)

Figure 5.5. SIFs vs d/a ratio. $K_0 = \sigma \sqrt{\pi a}$

d/a < 1.0 while $K_{II}$ continues a moderate increase as d/a changes from 1.0 to .25. Mode I, Isida's analytical results [75], shows an increasing trend with decreasing (d/a). While the results for the Mode I case agree very well with the analytical solution of Isida, only the BEM method was available to compare to a mixed mode problem and for eccentrically-loaded crack. For a mixed mode of a symmetrical crack, Wilson's [67] results show increasing values for both $K_I$ and $K_{II}$ as d/a decreases. For mode II there is week indication that the boundary collocation results fellow similar trends. On the other hand, mode I results indicates no definite increase in the range studied for d/a (.25, 1.0).

## B. Effects of Crack Angle on the SIFs

Figure 5.6 shows that the mixed mode stress intensity factors depend on the crack angle $\beta$. From the graph, it is apparent that the Mode II stress intensity factor decreases with increasing $\beta$, while Mode I stress intensity factor, $K_I$, increases with increasing $\beta$. The results of $\beta$ = 90 degree (Figure 5.4) is in excellent agreement with that of Isida [75]. As $\beta$ increases, the model approaches Mode I and $K_I$ is expected to increase. The opposite is also true, as $\beta$ decreases, $K_{II}$ increases. The boundary collocation method behave well in that it correctly accounts for the dependence of the SIFs on $\beta$. The literature is void of results to compare for mixed mode problems for eccentrically loaded cracks. We are limited to comparing our results to the BEM method. The results presented in (Figure 5.5) show an agreement for

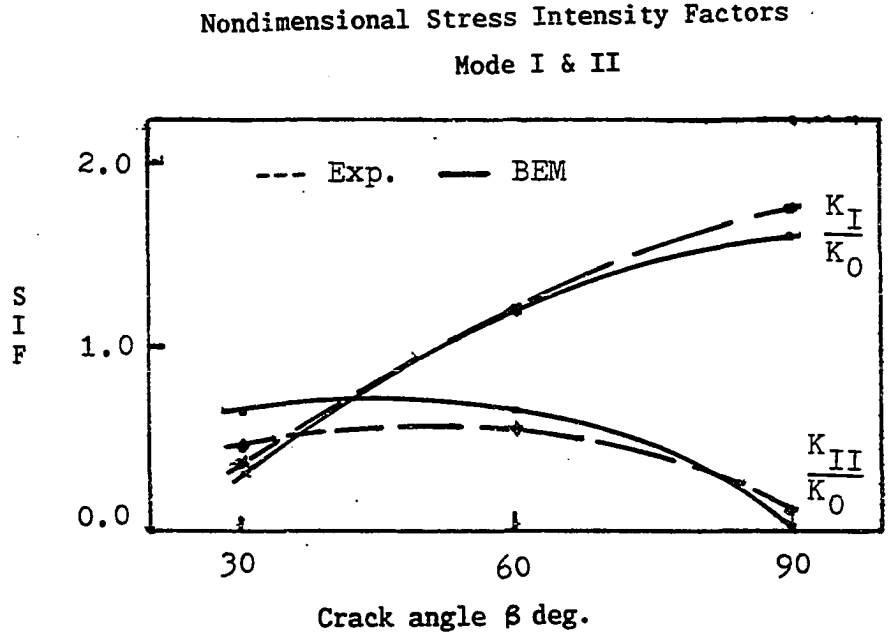


Figure 5.6. SIFs vs crack angle. $K_0 = \sigma \sqrt{\pi a}$

ratios (d/a) .25-1.0.

The boundary collocation method used in this research demonstrated its ability to handle moderate boundary interactions.

For Mode I and 0.4<d/a<1.0, the result are in good agreement with the boundary element method (BEM) numerical solution [74] (within 4%-13%). For Mode II, there is less agreement (5%-21%) with the BEM method. It is in excellent agreement with Isida [75] (within 2%) for pure Mode I. Since BEM was the only numerical method available to us, the only other check we had was back plotting. Figures 5.1 and 5.2 show that we can not confirm, from back plotting, if our results are acceptable. For the back plot to be acceptable (to have perfect match), we need to estimate all the terms entering the back plot very accurately. On the other hand, only the singular terms need to converge accurately to determine the fracture parameters. Similarly, the back plots were not acceptable for the other models, even when the results, $K_I$ and $K_{II}$, were in agreement with the numerical results.

It was not possible to determine the best results from back plotting. The best results were obtained from the smallest combination of terms where if one series order is increased, there is little change in the value of $K_I$ and $K_{II}$.

The results, though very weak for $K_I$, show increasing trend for the SIFs with decreasing (d/a) ratio. Mode I is in agreement with the results of Kobayashi et al. [65] for a central crack in Mode I and Srawley et al. [58] results for an edge crack in Mode I. Srawley et al. confirmed their results by experimentally measuring the compliance in an edge cracked specimen. These results agreed that for d/a < .4, there

was increase in the value of $K_I$ as the crack approaches the boundary (Figure 5.5). The change in $K_I$ and $K_{II}$ presented by the boundary collocation method are in line with previous works and BEM. The BEM used to compare our results was based on Erdogan's [76] equations for a point force in an infinite plate which was adopted for finite plates problems.

# VI. CONCLUSIONS

The boundary collocation method used in this research is easy to apply. Combined with an image analysis system, the task of specifying the location of boundary points is simple. The method is applicable when the state of stress can be fully described at the boundary points and the stress gradient is small. In these cases, the boundary collocation converges very quickly. It is a smaller system of linear equations, which can be solved on a small computer. Since most numerical methods are massive mathematical models which require, in general, mainframe computers are expensive to solve. A complex geometry poses no serious problem to boundary collocation. Yet, for numerical methods, this could become a formidable task. The local collocation of a few points on the boundary can accurately predict the value of the stress intensity factors. It is necessary to determine all the coefficients to allow generation of good back plots.

The ability of comparing back plots to an actual fringe field gives a more definite means of verifying the solution yet we were not able to do so.

Combining half fringe photoelasticity and an image analysis system makes data collection fast, easy and very accurate permitting usage of very small loads and the possibility of using modeling materials of lower bifringence constants. The image analysis system, allows collecting data from a boundary more accurately than it was possible at any time before.

Finally, it is possible to apply this method to a larger class of boundary shapes and to cracks interacting with other cracks as well.

## VII. BIBLIOGRAPHY


1. C. E. Inglis. "Stresses in a plate due to the presence of cracks and sharp corners." Transactions of the Royal Institution of Naval Architects, London, England, 60 (1913), 219-230.

2. A. A. Griffith. "The phenomena of rupture and flow in solids." Philosophical Transactions of the Royal Society of London, England, 221 (1921), 163-198.

3. H. M. Westergaard. "Stresses at a crack, size of the crack and the bending of reinforced concrete." Proceedings of the American Concrete Institute, 30 (1934), 93-102.

4. S. C. Hollister. "Experimental study of stresses at a crack in a compression member." Proceedings of the American Concrete Institute, 30 (1934), 361-365.

5. H. M. Westergaard. "Bearing pressures and cracks." Journal of Applied Mechanics, Trans. ASME, 61 (1939), A(49-53).

6. M. L. Williams. "Stress singularities resulting from various boundary conditions in angular corners of plates in extension." Journal of Applied Mechanics, Trans. ASME, 74 (1952), 526-528.

7. D. Post. "Photoelastic stress analysis for an edge crack in a tensile field." Proceedings of the Society for Experimental Stress Analysis, 12, No. 1 (1954), 99-116.

8. P. S. Theocaris and D. Pazis. "The topography of the core region around cracks under Modes I, II, and III of fracture." International Journal Mechanical Science, 25, No. 2 (1983), 121-136.

9. G. R. Irwin. "Analysis of stresses and strains near the end of a crack traversing a plate." Journal of Applied Mechanics, 24 (1957), 361-364.

10. D. P. Rooke and D. J. Cartwright. Compendium of Stress Intensity Factors. London: HMSO, 1976.

11. H. Tada, P. C. Paris, and G. R. Irwin. The Stress Analysis of Cracks Handbook. Hellertown, Pennsylvania: Del Research Corp., 1973.

12. P. C. Paris and G. C. Sih. "Stress analysis of cracks." Fracture Toughness Testing and its Application, ASTM STP 381 (1965), 30-83.

13. A. Wells and D. Post. "The dynamic stress distribution surrounding a running crack-a photoelastic analysis." Proceedings of SESA, 16, No. 1 (1958), 69-92.

14. H. Fessler and D. O. Mansell. "Photoelastic study of stresses near cracks in thick plates." Journal of Mechanical Engineering, 12, No. 3 (1962), 213-225.

15. R. H. Marloff, M. M. Leven, R. L. Johnson and T. N. Ringler. "Photoelastic determination of stress intensity factors." Experimental Mechanics, 11, No. 12 (1971), 529-539.

16. M. A. Schroedl, J. J. McGowen and C. W. Smith. "An assessment of factors influencing data obtained by photoelastic stress freezing technique for stress fields near crack tips." Journal of Engineering Fracture Mechanics, 4, No. 4 (1972), 801-809.

17. C. W. Smith. "Use of three-dimensional photoelasticity in fracture mechanics." Experimental Mechanics, 13, No. 12 (1973), 539-544.

18. C. W. Smith. "Photoelasticity in fracture mechanics." Experimental Mechanics, 20, No. 11 (1980), 390-396.

19. C. W. Smith and O. Olaosebikan. "On the extraction of mixed mode stress intensity factors from near tip photoelastic data in three-dimensional problems." Proceedings of 5th International Congress on Experimental Mechanics, Montreal, Canada, June 10-15, 1984.

20. C. W. Smith and O. Olaosebikan. "On the extraction of stress intensity factors from near tip photoelastic data." SESA Spring Conference Proceedings, Cleveland, Ohio, May 15-20, 1983, 7-15.

21. T. H. Baek. "Analysis of the interacting effect of double surface cracks by 3-dimensional photoelastic experiment." M.S. thesis, Iowa State University, Ames, Iowa, 1984.

22. C. W. Smith, J. J. MC Gowan and W. H. Peters. "A study of crack tip nonlinearities in frozen-stress fields." Experimental Mechanics, 18, August 1978, 309-315.

23. W. B. Bradley and A. S. Kobayashi. "An investigation of propagating cracks by dynamic photoelasticity." Experimental Mechanics, 10, No. 3 (1970), 106-113.

24. W. B. Bradley and A. S. Kobayashi. "Fracture dynamics-A photoelastic investigation." Engineering Fracture Mechanics, 3, No. 3 (1971), 317-332.

25. A. S. Kobayashi and M. Ramulu. "Dynamic stress intensity-factors for unsymmetrical isochromatics." Experimental Mechanics, 21, No. 1 (1981), 41-48.

26. A. S. Kobayashi and M. Ramulu. "Dynamic crack curving-A photoelastic evaluation." Experimental Mechanics, 23, No. 1 (1983), 1-9.

27. W. Wang. "Transient thermal stress intensity factors of near surface cracks." Ph.D. dissertation, Iowa State University, Ames, Iowa, 1985.

28. A. S. Redner. "Experimental determination of stress intensity factors. A review of photoelastic approaches." In Fracture Mechanics and Technology, 1, Eds. by G. C. Sih and C. L. Chow. Alphen aan den Rijn. The Netherlands: Sijthoff and Noordhoff international Publishers, 1977, pp. 607-622.

29. C. Ruiz and Y. P. Phang. "Stress intensity for interacting flaws -Part 3: Photoelastic determination of mixed mode stress intensity factors for interacting flaws." OUEL - 1368/81, University of Oxford, Oxford, England (1981).

30. G. R. Irwin. Discussion of reference 13. Proceedings of SESA, 16 No. 1 (1958), 93-96.

31. J. M. Etheridge and J. W. Dally. "A three-parameter method for determining stress intensity factors from isochromatic fringe loops." Journal of Strain Analysis, 13, No. 2 (1978), 91-94.

32. E. E. Gdoutos and P. S. Theocaris. "A photoelastic determination of mixed-mode stress intensity factors." Experimental Mechanics, 18, No. 3 (1978), 87-96.

33. R. H. Marloff, M. M. Leven, T. N. Ringler and R. L. Johnson. "Photoelastic determination of stress intensity factors." Experimental Mechanics, 11, No. 12 (1971), 529-539.

34. N. S. Murthy and P. R. Rao. "Photoelastic determination of mode I stress intensity factor in tensile strips-effect of crack length." Engineering Fracture Mechanics, 20, No. 3 (1985), 475-478.

35. D. Broek. Elementary Engineering Fracture Mechanics. Sijhoff and Noordhoff: Amsterdam (1978).

36. B. Gross and J. E. Srawely and W. F. Brown. "Stress intensity factors for a single edge notch tension specimen by boundary collocation of a stress function." NASA TN D-2395, Aug. 1964.

37. Y. F. Cheng. "Simultaneous determination of the first and second mode stress intensity factors." International Journal of Fracture Mechanics, 7, No. 1 (1971), 119-121.

38. R. J. Sanford. "Application of the least-square method to photoelastic analysis." Experimental Mechanics, 20, No. 6 (1980), 192-197.

39. R. J. Sanford and J. W. Dally. "A general method for determining mixed-mode stress intensity factors from isochromatic fringe patterns." Engineering Fracture Mechanics, 11, No. 4 (1979), 621-633.

40. J. W. Holmes, R. A. Holmes and J. C. Conway, Jr. "Determination of mode I stress intensity factors in surface-flawed plates by scattered-light photoelasticity." Journal of Strain Analysis, 18, No. 3 (1983), 173-176.

41. E. L. Ross, G. Kaminski and J. C. Conway. "Measurement of mode I stress intensity factors by scattered light photoelasticity." Experimental Mechanics, 22 (1982), 117-120.

42. J. Brillaud and A. Lagarde. "Ellipsometry in scattered light and its application to the determination of optical characteristic of a thin slice in tridimensional photoelasticity." Proceedings of the IUTAM Symposium on Optical Methods in Mechanics of Solids, sept. 10-14, 1979, Alphen aan den Rijn. The Netherlands: Sijthoff and Noordhoff Publishers, 1981, pp. 55-76,

43. A. S. Voloshin and C. P. Burger. "Half-fringe photoelasticity: A new approach to whole-field stress analysis." Experimental Mechanics, 23, Sept. 1983, 304-313.

44. R. K. Muller and L. Saackel. "Complete automatic analysis of photoelastic fringes." Presented at the 1978 SESA Spring Meeting, Wichita, Kansas, May 14-19.

45. C. L. Tsai and S. K. Park. "Determination of stress-intensity factors of fillet welded T-joints by computer-assisted photoelasticity." Experimental Mechanics, 24, No. 3 (1984), 233-242.

46. J. W. Dally and W. F. Riley. Experimental Stress Analysis. Second Edition. New York: McGraw-Hill Book Company, 1978.

47. M. Vandaele-Dossche and R. Van Green: La Bire'fringence Me'canique en Lumie're Ultra-Violette et ses Applications, Bull. Classe Sci. Acad., 50, No. 2(1964), 125-141.

48. R. N. Kar. "Stress intensity factors in glass plates with edge cracks by half fringe photoelasticity." M.S. thesis, Iowa State University, Ames, Iowa, 1977.

49. D. Mallik. "Reflective half fringe photoelasticity applied to adhesive joints." M.S. thesis, Iowa State University, Ames, Iowa, 1983.

50. A. E. H. Love. Treatise on the Mathematical Theory of Elasticity Fourth Edition. New York: Dover Publications, 1944.

51. N. I. Muskhelishvili. Some Basic Problems of the Mathematical Theory of Elasticity. Leyden, Netherland: International Publishing, 1975.

52. I. N. Sneddon and M. Lowengrub. Crack Problems in the Classical Theory of Elasticity. New York: John Wiley & Sons, Inc., 1969.

53. M. L. Williams. "On the stress distribution at the base of a stationary crack." Journal of Applied Mech., 24, March 1957, 109-114.

54. G. C. Sih. "On the westergaard method of crack analysis." International Journal of Fracture Mechanics, 2, No. 4 (1966), 628-631.

55. W. T. Evans and A. R. Luxmoore. "Limitation of the westergaard equations for experimental evaluation of stress intensity factors." Journal of Strain Analysis, 11, No. 3 (1976), 177-185.

56. J. Eftis and H. Liebowitz. "On the modified westergaard equations for certain plane crack problems." International Journal of Fracture Mechanics, 8, No. 4 (1972), 383-392.

57. B. Cotterell. "Notes on the paths and stability of cracks." international journal of fracture mechanics, 2, no. 3 (1966), 526-533.

58. J. E. Srawley, M. H. Jones, and B. Gross. "Experimental determination of the dependence of crack extension force on crack length for a single-edge-notch tension specimen." NASA TN D-2396, Aug. 1964.

59. P. S. Theocaris and E. E. Gdoutos. "A photoelastic determination of KI stress intensity factors." Engineering Fracture Mechanics, 7, No. 2 (1975), 331-339.

60. R. J. Sanford. "A critical re-examination of the westergaard method for solving opening-mode crack problems." Mechanics Research Communications, 6 (1979), 289-294.

61. J. W. Dally and R. J. Sanford. "Classification of stress-intensity factors from isochromatic-fringe patterns." Experimental Mechanics, 18, No. 12 (1978), 441-448.

62. H. P. Rossmanith. "A hybrid technique for improved K determination from photoelastic data." Experimental Mechanics, 23, June 1983, 152-157.

63. M. Cottron and A. Lagarde. "A far-field method for the determination of mixed-mode stress-intensity factors from isochromatic fringe patterns." Solid Mechanics Archives, 7, Issue 1 (1982), 1-18.

64. J. Eftis, N. Subramonian, and H. Liebowitz. "Crack border stress and displacement equations revisited." Engineering Fracture Mechanics, 9 (1977), 189-210.

65. A. S. Kobayashi, R. D. Cherepy, and W. C. Kinsel. "A numerical procedure for estimating the stress intensity factor of a crack in a finite plate." Journal of Basic Engineering, Trans. ASME, Series D, 86, NO. 4 ( Dec. 1964), 681-684.

66. J. V. Vooren. "Remarks on an existing numerical method to estimate the stress intensity factor of a straight crack in a finite plate." Journal of Basic Engineering, Trans. ASME, Series D, 89, No.1 ( Mar. 1967), 236.

67. W. K. Wilson. "Numerical method for determining stress intensity factors of an interior crack in a finite plate." Trans. ASME, Ser. D, 93, No. 4 (1971), 685-690.

68. V. Z. Parton and E. M. Morozov. Elastic-Plastic Fracture Mechanics. English Translation, Moscow: Mir Publishers, 1978.

69. G. L. Cloud. "Mechanical-optical characteristics of polycarbonate and relationships with materials structure." Presented at 1968 SESA Fall Meeting San Francisco, Calif, Oct. 28, No. 1, Exp. Stress Analysis.

70. J. W. Dally and A. Mulc. "Polycarbonate as a model material for three-dimensional photoplasticity" Journal of Applied Mechanics, Trans. ASME, June 73, 600-606.

71. EyeCom II Handbook. Second Edition. Goleta, CA: Spatial Data Systems, Inc., 1980.

72. I. Miskiglu. Program Bank. Department of Engineering Science and Mechanics, Iowa State University, Ames, Iowa, 1986.

73. H. Y. Lee Jonah. Program Bank. Department of Engineering Science and Mechanics, Iowa State University, Ames, Iowa, 1980.

74. L. S. Koo. "The solution of multiple, interacting crack problems by the boundary integral equation method." M.S. thesis, Iowa State University, Ames, Iowa, 1983.

75. M. Isida. "Stress-intensity factor for the tension of an eccentrically cracked strip." Journal of Applied Mechanics, 33, Sept. 1966, 624-625.

76. F. Erdogan. "On the stress distribution in plates with collinear cuts under arbitrary loads." Proceedings of the Fourth U. S. National Congress of Applied Mechanics, ASME, 1 (1962), 547-553.

## VIII. ACKNOWLEDGEMENTS

It is with appreciation that I acknowledge the valuable opportunity to work with Dr. Christian P. Burger. As my major professor, his knowledge and experience contributed greatly to my professional growth. His interest in my work was a source of encouragement.

I would like also to thank Professors J. C. Huston, W. L. Larsen, W. F. Riley, and S. Bahadur. I am grateful for their advice and service as my committee members.

I would also like to give special thanks to Dr. I. Miskioglu, who introduced me to the EyeCom system and provided me with the calibration routine CAL2A. He was of great assistance.

I also would like to extend my thanks to Mr. Bruce H. Koerner. I appreciate his valuable suggestions on advanced programming.

The financial support from the Department of Engineering Science and Mechanics is very much appreciated.

Finally, I would like to acknowledge the continuous support my wife and family members gave me. Their support helped make this task possible. To all of them, my warmest thanks, love, and devotion.